The Astrophysical Journal, 888:97 (18pp), 2020 January 10 https://doi.org/10.3847/1538-4357/ab5fd6

Thermal Evolution of Neo-neutron Stars. I. Envelopes, Eddington Luminosity Phase, and Implications for GW170817

Mikhail V. Beznogov[1], Dany Page[1], and Enrico Ramirez-Ruiz[2,3]
[1] Instituto de Astronomía, Universidad Nacional Autónoma de México, Ciudad de México, 04510, Mexico; mikhail@astro.unam.mx, page@astro.unam.mx
[2] Department of Astronomy and Astrophysics, University of California, Santa Cruz, CA 95064, USA
[3] Niels Bohr Institute, University of Copenhagen, Blegdamsvej 17, DK-2100 Copenhagen, Denmark; enrico@ucolick.org

Received 2019 August 20; revised 2019 December 5; accepted 2019 December 6; published 2020 January 14

Abstract

A neo-neutron star is a hot neutron star that has just become transparent to neutrinos. In a core-collapse supernova or accretion-induced collapse of a white dwarf, the neo-neutron star phase directly follows the proto-neutron star phase, about 30–60 s after the initial collapse. It will also be present in a binary neutron star merger in the case where the "born-again" hot massive compact star does not immediately collapse into a black hole. Eddington or even super-Eddington luminosities are present for some time. A neo-neutron star produced in a core-collapse supernova is not directly observable, but the one produced by a binary merger, likely associated with an off-axis short gamma-ray burst, may be observable for some time as well as when produced in the accretion-induced collapse of a white dwarf. We present a first step in the study of this neo-neutron star phase in a spherically symmetric configuration, thus ignoring fast rotation and also ignoring the effect of strong magnetic fields. We put particular emphasis on determining how long the star can sustain a near-Eddington luminosity and also show the importance of positrons and contraction energy during the neo-neutron star phase. We finally discuss the observational prospects for neutron star mergers triggered by LIGO and for accretion-induced collapse transients.

Unified Astronomy Thesaurus concepts: Neutron stars (1108); Type II supernovae (1731); Gamma-ray bursts (629); X-ray point sources (1270)

1. Introduction

Neutron stars are by far the most intriguing objects in the universe. They are superdense, can be superfast rotators, may have superstrong magnetic fields, and are surrounded by the strongest gravitational fields (see, e.g., Haensel et al. 2007). They are born in core-collapse supernova events (Baade & Zwicky 1934) or in accretion-induced collapse of white dwarfs (Canal & Schatzman 1976), and start their life as proto-neutron stars (Burrows & Lattimer 1986). Moreover, a hot born-again massive neutron star may also be produced in the merging of a binary neutron star system and survive as such (Kluźniak & Ruderman 1998), or collapse into a black hole. During the first hot phase, neutrinos are copiously produced but are trapped in the stellar interior and only escape by slowly diffusing outward. This early evolution, lasting less than a minute, has been extensively studied theoretically, in large part because a Galactic core-collapse supernova would allow us to follow it observationally through the detection of the emitted neutrinos. The subsequent phase, which we will call the neo-neutron star phase, from an age of a minute after the birth/rebirth to a few hours/days, has, however, never been carefully considered. Later phases have been the object of numerous studies (see, e.g., Yakovlev & Pethick 2004; Page et al. 2006).

After the supernova, it may take decades until the ejecta become transparent to electromagnetic radiation from the central object (Bahcall et al. 1970). In the case of the supernova SN 1987A, it was only recently, after more than 30 years, that credible evidence of the presence of a compact object has been found (Cigan et al. 2019). The youngest observed neutron star is the compact object in the center of the Cassiopeia A supernova remnant (Tananbaum 1999), with an age of about 340 yr (Fesen et al. 2006). It is thus doubtful we will have, in the near future, valuable observational data on the very early cooling history of a neutron star, and even less of a neo-neutron star. The neo-neutron phase is, however, the phase during which the neutron star crust is formed, and it is, thus, establishing the basic structure for a large amount of neutron star phenomenology.

A complementary setup is provided by binary neutron star mergers (Lee & Ramirez-Ruiz 2007; Faber & Rasio 2012). Although it is often considered that the outcome of such event would be the formation of a low-mass black hole (Eichler et al. 1989; Rezzolla et al. 2011; Murguia-Berthier et al. 2014), there is a possibility that the merged object survives as a massive neutron star (Usov 1992; Kluźniak & Ruderman 1998; Metzger et al. 2008). In such a scenario, we would have a "born-again" neutron star, with trapped neutrinos because of its high temperature, followed by a massive neo-neutron star. This possibility is real only if the high-density equation of state (EOS) is stiff enough to have a high maximum mass, $M_{\max}$. The maximum mass of a cold slowly or nonrotating neutron star is at least 2 $M_\odot$, from the masses of the pulsars PSR J1614–2230 (Demorest et al. 2010) and PSR J0348+0432 (Antoniadis et al. 2013) and possibly higher than 2.3 $M_\odot$ from the upper value of the mass of PSR J0740+6620 (Cromartie et al. 2019). Analyses of the GW170817/GRB 170817A gravitational wave/gamma-ray burst event have also provided new constraints on $M_{\max}$ based on the delayed collapse of the merged object into a black hole. Margalit & Metzger (2017) obtain $M_{\max} \leqslant 2.17\ M_\odot$ (90%), and Rezzolla et al. (2018) find $2\ M_\odot \leqslant M_{\max} \leqslant 2.3\ M_\odot$ while the more detailed study of Shibata et al. (2019) conclude that $M_{\max} \leqslant 2.3\ M_\odot$. If such is the case, only mergers of binaries containing low-mass neutron stars could produce a stable merged object so that our neo-neutron star description would be of interest.

As a first step, in the present paper, we consider the evolution of the outer layer of the neo-neutron star, its envelope, just after the formation of nuclei when the surface temperature is high enough to be of the order of the Eddington luminosity, i.e., of the order of $10^{38}\,\mathrm{erg\,s^{-1}}$. An important question we tackle is the duration of a possible Eddington or super-Eddington phase and then consider the subsequent evolution. Based on previous studies of proto-neutron stars, we explore the impact of different possible initial temperature/luminosity profiles in the envelope on the Eddington phase.

This paper is structured as follows. In Sections 2 and 3, we set up the problem and present our results on the low-density regime of an Eddington envelope. In Section 4, we define what a neo-neutron star phase is and contrast the method for studying long-term cooling of isolated neutron stars versus the neo-neutron star case. Our resulted are described in Section 5, and their observational relevance is discussed in Section 6. A summary and conclusions are presented in Section 7. Finally, in Appendices A and B, we describe the physical properties of hot neutron star envelopes, and our numerical scheme is detailed in Appendix C.

2. Thermal Evolution Equations

We consider a spherically symmetric problem, ignoring the effects of rotation and magnetic fields. Because the structure of the outer layers of our stars will expand or contract, we employ the enclosed baryon number a as a (Lagrange) radial variable instead of the circumferential radius r. The full set of general relativistic structure and mechanical evolution equations can be found, e.g., in Potekhin & Chabrier (2018). The thermal evolution equations we will solve are

$$\widetilde{L} = -K(4\pi r^2)^2 n e^{\phi}\frac{\partial \widetilde{T}}{\partial a}, \tag{1}$$

$$e^{\phi}\frac{\partial(\widetilde{T}e^{-\phi})}{\partial t} = -\frac{1}{C_{\mathrm{V}}}(\widetilde{Q}_{\mathrm{L}} + \widetilde{Q}_{\nu} + \widetilde{Q}_{\mathrm{V}}), \tag{2}$$

where $\widetilde{L} = Le^{2\phi}$ and $\widetilde{T} = Te^{\phi}$ are the redshifted luminosity and temperature, respectively, $e^{2\phi}$ being the time component of the metric. C_{V} is the heat capacity and K the thermal conductivity. The energy sources/sinks are

$$\widetilde{Q}_{\mathrm{L}} \equiv n\frac{\partial \widetilde{L}}{\partial a}, \tag{3}$$

which gives the heat loss/injection from the luminosity gradient, $\widetilde{Q}_{\nu} = e^{2\phi}Q_{\nu}$, which gives the neutrino energy loss, and

$$\widetilde{Q}_{\mathrm{V}} \equiv -\widetilde{T}\left(\frac{\partial P}{\partial T}\right)\bigg|_{n}\frac{\partial \ln n}{\partial t}, \tag{4}$$

which will be called the contraction energy. This last term comes from the "$P\,dV$" work and the volume-dependent part of the internal energy, and gives the gravitational and internal energy release owing to the contraction of the star during its cooling.

We follow the evolution of the star with a sequence of models in hydrostatic equilibrium, i.e., we ignore acceleration compared to gravity. We have explicitly checked that our results are consistent with this approximation.

The microphysics we employ is standard, and we describe it in Appendices A and B.

3. Outer Boundary and Envelope

Boundary conditions at the center, where $a = 0$, are obvious:

$$\widetilde{L}(0) = 0, \quad r(0) = 0, \quad m(0) = 0, \tag{5}$$

while $P(a = 0) \equiv P_{\mathrm{c}}$ is an arbitrary parameter that will determine the mass of the star. Boundary conditions at the surface are more delicate, and "surface" must be properly defined. The simplest and naive condition is the "zero condition": $P_{\mathrm{s}} = \rho_{\mathrm{s}} = T_{\mathrm{s}} = 0$, and one takes $R \equiv r_{\mathrm{s}}$ and $M \equiv m_{\mathrm{s}}$. The subscript "s" refers to the quantities at the surface. However, this is too naive because P, ρ, and T, likely never really reach zero and, more likely, there is a smooth transition from the stellar interior to the surrounding magnetosphere (or the interstellar medium in the case of a nonmagnetized star). It is more appropriate, when studying the thermal evolution of the star, to define its surface as located at the photosphere, i.e., the layer where the outflowing thermal radiation is produced. We adopt the commonly used Eddington, or photospheric, condition (see, e.g., Hansen et al. 2004), in which detailed radiative transfer (where the energy dependence of the opacity is wholly taken into account) is replaced by a diffusion approximation (where the energy-dependent opacity is replaced by its Rosseland mean), i.e., the same Equation (1), and the photosphere is defined as the layer where the optical depth is $2/3$. This lead to the conditions

$$L_{\mathrm{s}} = 4\pi\sigma_{\mathrm{SB}}R^2T_{\mathrm{s}}^4 \tag{6}$$

and

$$P_{\mathrm{s}} = \frac{2}{3}\frac{g_{\mathrm{s}}}{\kappa_{\mathrm{s}}}\left(1 + \frac{L_{\mathrm{s}}}{L_{\mathrm{Edd}}}\right), \tag{7}$$

where

$$g_{\mathrm{s}} = e^{\lambda}\,GM/R^2 \tag{8}$$

is the free-fall acceleration at the surface, $e^{2\lambda}$ being the radial component of the metric, σ_{SB} the Stephan–Boltzmann constant, κ_{s} the Rosseland mean opacity at the surface, and

$$L_{\mathrm{Edd}}(R) = \frac{4\pi c\,GMe^{\lambda}}{\kappa_{\mathrm{s}}} = \frac{4\pi R^2\,c\,g_{\mathrm{s}}}{\kappa_{\mathrm{s}}} \tag{9}$$

the Eddington luminosity at the stellar surface.

These are then complemented by the obvious relations that define the mass M and radius R of the star,

$$M = m_{\mathrm{s}} \quad \text{and} \quad R = r_{\mathrm{s}}, \tag{10}$$

and the continuity of the metric coefficient with the external Schwarzschild solution

$$e^{\phi(R)} = e^{-\lambda(R)} = \sqrt{1 - 2GM/Rc^2}. \tag{11}$$

It is numerically inconvenient to directly apply the outer boundary conditions of Equations (6) and (7), and we rather apply the standard scheme of separating out an envelope (Gudmundsson et al. 1982) as described below.

In these outer layers, the equation of hydrostatic equilibrium is simply

$$\frac{dP}{dl} = -g_{\mathrm{s}}\rho \tag{12}$$

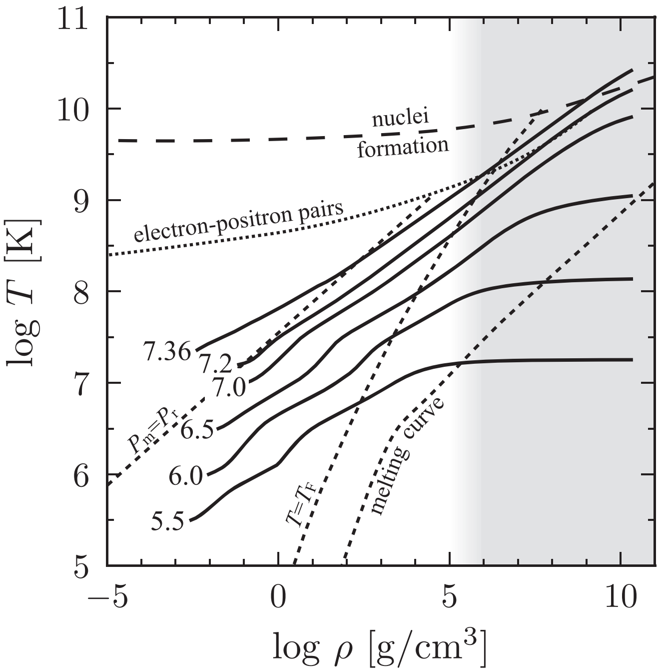

Figure 1. Envelope temperature profiles for six surfaces temperature, as labeled by log T_s. ($g_s = 10^{14}$ cm s^{-2} is assumed.) See details in the text. The gray shadowed part above 10^5 g cm^{-3} is shown for illustration but not used in our evolutionary calculations.

when written in terms of the proper radial length l, which is defined through $dl \equiv e^{-\lambda(r)}dr$. From a given layer at ρ_a and P_a, hydrostatic equilibrium can be integrated outward, giving the well-known classical result

$$P_a = y_a\, g_a \quad \text{with} \quad y_a \equiv \int_a^\infty \rho(r)dl \tag{13}$$

being the proper column density of matter above point "a," and where it has been assumed that the upper layers are sufficiently concentrated that g can be considered constant. In practice, we can replace g_a by g_s.

3.1. High-luminosity Envelopes

The envelope is defined as the outer layers, from the surface down to a bottom layer at some pressure P_b or, equivalently, density ρ_b, in which the EOS is temperature dependent and thus requires special treatment compared to the highly degenerate interior. For our present purpose, we extended the previous models of Beznogov et al. (2016) to higher temperatures by adding radiation pressure to the EOS of fully ionized plasma of Potekhin & Chabrier (2010)[4] and by adding the $L_s/L_{\rm Edd}$ term to the surface condition as in Equation (7). As we justify below in Section 4, we restrict ourselves to envelopes made of pure iron.

Figure 1 shows six envelope temperature profiles labeled by log T_s and the locations of several critical loci: the melting curve (i.e., ions form a Coulomb crystal at densities above this curve), the appearance of electron–positron pairs, the onset of electron degeneracy (labeled as "$T = T_F$"), the transition from matter- to radiation-pressure-dominated regimes (labeled as "$P_m = P_r$"), and the temperature below which nuclei are formed (Lattimer & Swesty 1991). One can also see that the profiles with the highest temperatures (log T_s (K) $>$ 7) cross the electron–positron pairs curve at a density of about 10^5 g cm^{-3} and also the nuclear formation/dissociation line when $T > 10^{10}$ K. Neither pairs nor nuclei dissociation is included in our envelope models, and these parts of the profiles should not be trusted. However, as discussed in Section 4, we will locate our outer boundary density ρ_b at 10^5 g cm^{-3}, and this regime of high-density inaccurately modeled envelopes will not be actually used and is plotted here only for illustrative purposes.

Notice that in the matter-dominated regime, and with opacity dominated by free–free-absorption, ρ_s increases with T_s while in the radiation-dominated regime, and opacity dominated by electron scattering, the relationship is inverted. One sees from Figure 1 that the transition between these two regimes occurs just above $T_s \sim 10^7$ K.

These envelope models provide us with a relationship between the temperature at the bottom of the envelope, T_b, and at its surface, T_s, the so-called "T_b–T_s relationship": $T_b = T_b(T_s)$. Because energy sources and sinks are ignored within the envelope, the luminosity at its bottom, L_b, is equal to the surface luminosity, and thus we obtain a relationship between the two searched-for solutions of Equations (1) and (2): $L_b = L_b(T_b)$. This allows us to replace the outer boundary condition $L_s = L_s(T_s)$ of Equation (6) at P_s by a new one applied deeper at P_b.

It was shown by Gudmundsson et al. (1982) that in the resulting relationship $T_s = T_s(T_b)$, the dependence on M and R is only through g_s in the form

$$T_s(T_b, g_{s,14}) = g_{s,14}^{1/4}\, T_s(T_b, g_{s,14} = 1), \tag{14}$$

where $g_{s,14} \equiv g_s/(10^{14}\,\text{cm s}^{-2})$. We have explicitly checked that this result is still valid for our hot envelopes with a lower density inner boundary at $\rho_b = 10^5$ g cm^{-3}.

We notice that the approximations that lead to the Eddington boundary condition of Equation (7) are actually self-inconsistent (Hansen et al. 2004), and the identification of a "surface" layer at temperature T_s has to be seen instead as a convenient ansatz for a more realistic atmospheric boundary condition. It is however well known (see, e.g., Kippenhahn et al. 2012) that envelope models will converge toward the "zero condition," and the exact definition of the "surface" is not important when studying the deeper layers. We will henceforth adopt the common notation of writing the outflowing luminosity in terms of an effective temperature $T_{\rm eff}$ as $L = 4\pi\sigma_{\rm SB}R^2T_{\rm eff}^4$ and use redshifted quantities as $L^\infty = 4\pi\sigma_{\rm SB}R_\infty^2 T_{\rm eff}^{\infty\,4}$ with $L^\infty \equiv e^{2\phi}L = \widetilde{L}_s$, $T_{\rm eff}^\infty \equiv e^\phi T_{\rm eff}$ and $R_\infty \equiv e^{-\phi}R$, and in our case $T_{\rm eff} = T_s$.

4. Neo-neutron Stars

The early evolution of a newly born, or a born-again, neutron star can be divided into two separate phases:

1. Proto-neutron star phase, $0 \leqslant t \lesssim 30$–$60$ s. The star is opaque to neutrinos, $T \gg 10^{10}$ K. The chemical composition of the core slowly evolves toward the zero-temperature one as neutrinos leak out and the star's lepton number decreases.
2. Neo-neutron star phase, 30–60 s $\lesssim$ t $\lesssim$ 1 days. The star becomes transparent to neutrinos, $T \ll 10^{11}$ K. The crust is being formed.

---

[4] The corresponding Fortran code is available at http://www.ioffe.ru/astro/EIP/.

The standard approach used in long-term cooling studies (Yakovlev & Pethick 2004; Page et al. 2006) needs adjustments to study neo-neutron stars as we are now interested in very short-term evolutions and very high temperatures. To be able to resolve short timescales, it becomes necessary to push the outer boundary to much lower densities, and we will typically use $\rho_{\rm b} = 10^5$ g cm^{-3}, resulting in an envelope with a thermal time of the order of a second. A direct consequence of this is that the outer layers of the interior have an EOS that becomes temperature dependent. We thus distinguish three regions:

1. Outer (heat-blanketing) envelope at densities $\rho_{\rm s} \leqslant \rho \leqslant \rho_{\rm b}$, treated separately in a time-independent way (see Section 3.1). It has Equations (6) and (7) as a surface boundary condition that defines $\rho_{\rm s}$, $P_{\rm s}$, and $T_{\rm s}$, for every given $L_{\rm s}$.
2. Inner envelope in the regime $\rho_{\rm b} \leqslant \rho \leqslant \rho_{\rm c}$ in which the EOS is still temperature dependent and where both structure and thermal equations have to be solved simultaneously. The outer envelope provides the outer boundary condition $L_{\rm b} = L_{\rm b}(T_{\rm b})$ for T and L, while for P and ρ, we use Equation (13) to write $P_{\rm b}\ (t) = g_{\rm b}(t)\ y_{\rm b}$, the time dependence coming from the contraction of this inner envelope. With the EOS, $T_{\rm b}(t)$ and $P_{\rm b}(t)$ give us $\rho_{\rm b}(t)$ (and even if $P_{\rm b}$ is constant, $\rho_{\rm b}$ will still change as long as $T_{\rm b}$ does). In the absence of mass loss, $y_{\rm b}$ is constant, which is what we will assume in the present work. The fact that both P and ρ, and consequently the radius r, change with time in the inner envelope is the reason we prefer to use the baryon number a, a conserved quantity, as radial variable.
3. Stellar interior at $\rho \geqslant \rho_{\rm c}$, where the EOS is temperature independent and only the thermal equations have to be solved at each time step.

Models of both proto-neutron stars (see, e.g., Burrows & Lattimer 1986) and neutron star mergers (see, e.g., Rosswog & Liebendörfer 2003) show that the star relaxes to a temperature of a few times 10^{10} K in less than a minute and so we will take as initial temperature $(2\text{–}3) \times 10^{10}$ K above $\rho_{\rm c}$. Taking $\rho_{\rm c} = 10^{11}$ g cm^{-3} as the inner boundary of the inner envelope is sufficient to guarantee that the stellar interior EOS can be considered as temperature independent. The microphysics we apply in the interior is the same as in long-term cooling models and was described in Page et al. (2004, 2011), while the microphysics of the inner envelope is described in Appendix A.

Numerically, solving the equations of mechanical structure and thermal evolution at very high temperatures where the radiation and pair pressure are significant in the inner envelope is much more challenging than in the later evolution. We describe in Appendix C the details of our solver.

5. Results

5.1. Initial Configurations

We begin our modeling once the star is transparent to neutrino, i.e., after the ~30 s long proto-neutron star phase in the case of a core-collapse supernova or after a similar duration after the fusion of the two stars in the case of a neutron star–neutron star merger (in the case where the merged object survives instead of having collapsed into a black hole). In both cases, the interior temperatures are of the order of $2\text{–}3 \times 10^{10}$ K (see, e.g., Pons et al. 1999 and Rosswog & Liebendörfer 2003). We will thus take as an initial temperature $T_0 \simeq 2.5 \times 10^{10}$ K at all densities above $\rho_{\rm c} = 10^{11}$ g cm^{-3}. At such densities, this T_0 is just below the transition temperature where nuclei are formed in the crust (Lattimer & Swesty 1991; see, e.g., Nakazato et al. 2018 for a proto-neutron star evolution study with formation of nuclei). We then introduce a temperature gradient in the inner envelope, from $\rho_{\rm c}$ down to $\rho_{\rm b} = 10^5$ g cm^{-3}, our initial outer boundary point. Numerical simulations of neither proto-neutron stars nor mergers resolve the temperature profile at low densities (outside the neutrinosphere), and we have thus no information about this outer layer temperature gradient. (Simulations of core-collapse supernovae do model the lower density layers but they typically follow the evolution of the system for less than a second; see, e.g., Janka 2012.) We want to start with a star emitting at the Eddington limit at its surface, and this uniquely fixes the initial temperature $T_{\rm b,0}$ at $\rho_{\rm b}$. The "Eddington effective temperature" $T_{\rm eff,Edd}$ is obtained (see Equation (9)) from $L_{\rm Edd} = 4\pi c\ GMe^{\lambda}/\kappa_{\rm s} = 4\pi R^2 c g_s/\kappa_{\rm s} \equiv 4\pi R^2 \sigma_{\rm B} T^4_{\rm eff,Edd}$ or

$$T_{\rm eff,Edd} = g_{\rm s}^{1/4}\left(\frac{c}{\sigma_{\rm B}\kappa_{\rm s}}\right)^{1/4} \tag{15}$$

while envelope models relate $T_{\rm eff}$ to $T_{\rm b}$ with the same $g_{\rm s}^{1/4}$ scaling (see Equation (14)), implying that the $T_{\rm b}$ resulting in an Eddington luminosity is a unique temperature, $T_{\rm b,Edd}$, determined by the boundary density $\rho_{\rm b}$ and the chemical composition of the envelope, but independent of M and R. For a pure iron envelope, we find that $T_{\rm b,Edd} = 1.07 \times 10^9$ K at $\rho_{\rm b} = 10^5$ g cm^{-3}.

We will consider three series of stellar models, with three different surface gravities, and implement in them different initial inner envelope luminosity or temperature profiles:

1. Models A, A′, B1, B2, B3, B4, and E, F: $M = 1.4\,M_\odot$ and $R \simeq 11.6$–11.8 km with $g_{\rm s,14} \simeq 1.6 - 1.7$.
2. Model C: $M = 2\,M_\odot$ and $R \simeq 11$ km with $g_{\rm s,14} \simeq 3.2$.
3. Models D and D′: $M = 0.25\,M_\odot$ and $R \simeq 17$–19 km with $g_{\rm s,14} \simeq 0.1$.

The quoted values of the radii come from our specific choice of the core EOS from Akmal et al. (1998). The last two models D and D′ are aimed at mimicking the effect of fast rotation where centrifugal acceleration can be seen as resulting in a small effective surface gravity: a complete treatment of rotations would need a 2D code, and our results are only intended to give a first approximation to the possible effects of fast rotation. In model C, we do not include the fast neutrino emission by the direct Urca process (Boguta 1981; Lattimer et al. 1991) acting deep in the inner core because it has no effect on the evolution of the outer parts of the star at early stages.

As explained in Appendix C, we find it more convenient numerically to define the initial luminosity profile, $L_0(\rho)$, in the envelope rather than directly defining T. We show in Figure 2(a) our choices: models A, B1, B2, B3, C, and D have $L = L_{\rm Edd}$ at $\rho_{\rm b}$, with the value of $L_{\rm Edd}$ for their corresponding M, and the variation of L with increasing density constrained so that T reaches $T_0 \simeq 2.5 \times 10^{10}$ K at $\rho_{\rm c} = 10^{11}$ g cm^{-3}. The model E is, in contradistinction, defined by the temperature profile, following Equation (23), and results

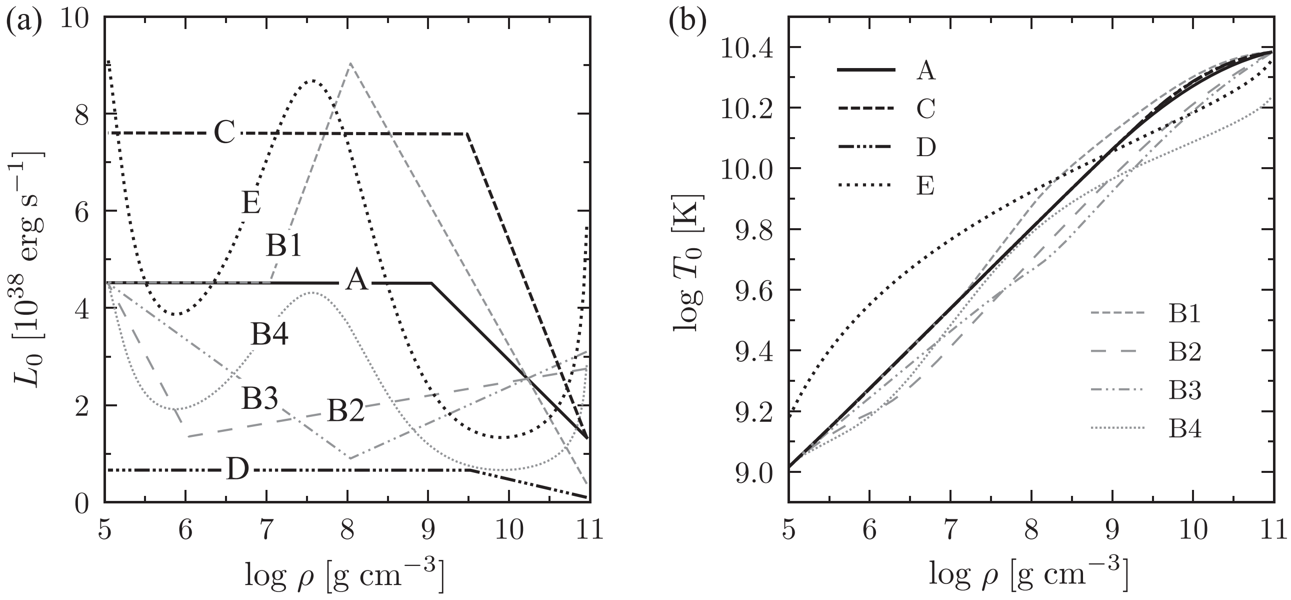

Figure 2. Panel (a): initial local luminosity profiles of all our models. Panel (b): corresponding initial local temperature profiles. See details in the text.

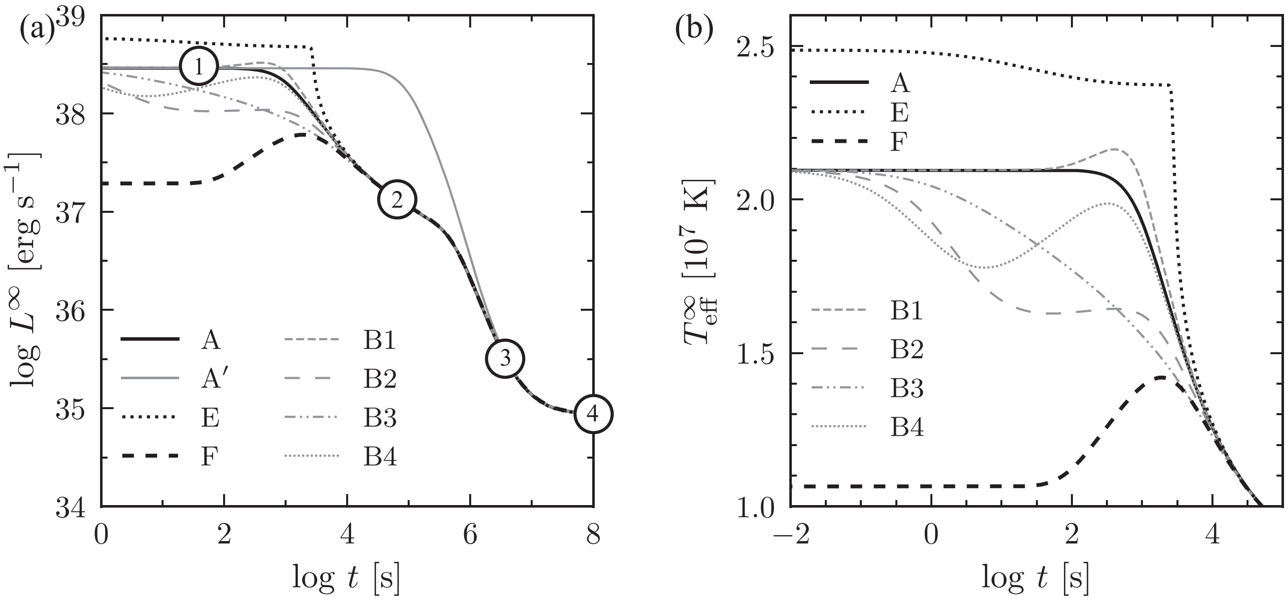

Figure 3. Cooling curves of our 1.4 $M_\odot$ models A, A′, B1, B2, B3, B4, and E, F. Panel (a) shows the redshifted luminosity L^∞ and panel (b) the redshifted effective temperature $T_{\rm eff}^\infty$. See details in the text.

in a super-Eddington L at the surface. Model B4 is obtained from the L profile of model E scaled down so that its resulting surface luminosity is again the Eddington one (but then it cannot reach T_0 at ρ_c). In Figure 2(b), we plot the corresponding temperature profiles. For the reason discussed above, all models with $L(\rho_b) = L_{\rm Edd}$ start at the same $T_{b,0} = T_{\rm b,Edd} = 1.07 \times 10^9$K, while the super-Eddington model E has a higher $T_{b,0}$.

Notice that because the total opacity κ is much smaller in the inner envelope than at the surface, the local Eddington luminosity $L_{\rm Edd}(r) = 4\pi r^2\, c g_s/\kappa$ is much larger than $L_{\rm Edd}(R)$ and, hence, in all models the luminosity in the inner envelope is always below $L_{\rm Edd}(r)$.

Finally, model F represents a cold start with an initial $T_{\rm eff}$ about twice lower and hence an initial surface luminosity about 15 times below $L_{\rm Edd}(R)$. To avoid saturating the figure, the initial L and T profiles of this model are not displayed in Figure 2.

5.2. Evolution of a 1.4 $M_\odot$ Star

The cooling curves resulting from our initial L and T profiles are presented in Figure 3 for our 1.4 $M_\odot$ case. One sees that all models converge, i.e., forget their initial conditions, in about 10^4 s (except model A′; see below) and this initial relaxation phase is denoted as phase "1." After this, during phase "2," the cooling is driven by neutrino emission from the pair-annihilation process and, after the knee,[5] at age $\sim 3 \times 10^5$ s, by neutrino from the plasmon decay process, phase "3." Model A′ has the same initial temperature and luminosity as model A but the neutrino emission by the pair-annihilation process has been arbitrarily turned off: this model confirms that pair annihilation is responsible for the evolution during phase

---

[5] This knee can already be seen in the results of Nomoto & Tsuruta (1987), but with no interpretation provided, and in Page (1989).

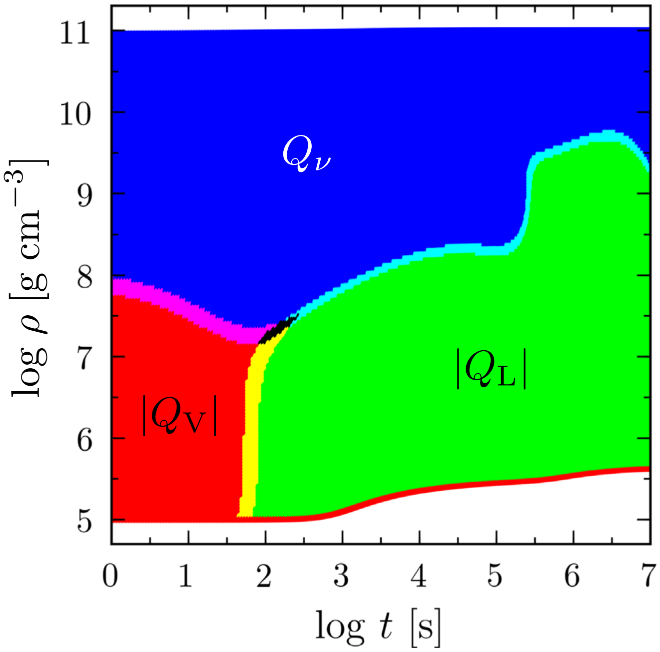

Figure 4. Plot of dominant energy term in the energy balance Equation (2) in model A: blue for Q_ν, red for $|Q_V|$, and green for $|Q_L|$; other colors are where two contributions are within 20% of each other while in the black region all three are within 20% of each other. (We use absolute values for the quantities Q_V and Q_L which can be either positive or negative.)

"2," while during phase "3" (driven by plasmon decay) model A′ converges toward model A. At an age of about one year, the luminosity, and the surface temperature, reaches a stagnation phase. Phase "4": this is the "early plateau," already well known in neutron star cooling studies, that will last for a few decades and corresponds to the thermal relaxation of the whole neutron star crust, which will eventually reach thermal equilibrium with the core (see Nomoto & Tsuruta 1987; Page 1989; Lattimer et al. 1994, and Gnedin et al. 2001). The shift from phase "3" to "4" is due to the inner envelope temperature dropping below the plasma temperature and the consequent exponential suppression of plasmon formation and decay: the main neutrino process available is then the very inefficient electron–ion bremsstrahlung resulting in a significant slowdown of the cooling.

In the right panel of Figure 3, we show a close up of the early evolution of $T_{\rm eff}^\infty$. It is interesting to notice here that these cooling curves map their initial temperature profiles that were displayed in Figure 2(b): it results from a mapping of $T_0(\rho)$ into $T_{\rm eff}(t)$. This mapping is good up to time $\sim 10^3$ s with ρ up to 10^8 g cm^{-3}: it was shown by Brown & Cumming (2009) that as long as $T_{\rm eff}^\infty$ is controlled by heat transport from deeper layers, its value is determined mostly by the initial $T_0(\rho)$ at a depth whose thermal diffusion timescale to the surface is equal to the time elapsed from when this initial $T_0(\rho)$ was set. In our case, the mapping ends when t–ρ reaches a density where the evolution is driven by neutrinos more than by heat diffusion toward the surface, and this happens when approaching the phase "2" dominated by pair-annihilation neutrinos. In Figure 4, we show the time evolution of the dominant energy term in the energy balance Equation (2) as a function of density for model A: the details of such a plot are dependent on the assumed initial T profile, but Q_ν eventually dominating at high densities (which, as one can see, turn out to be above $\sim 10^8$ g cm^{-3}) is a simple result of the high T dependence of neutrino processes and the strongly rising T profile as ρ increases.

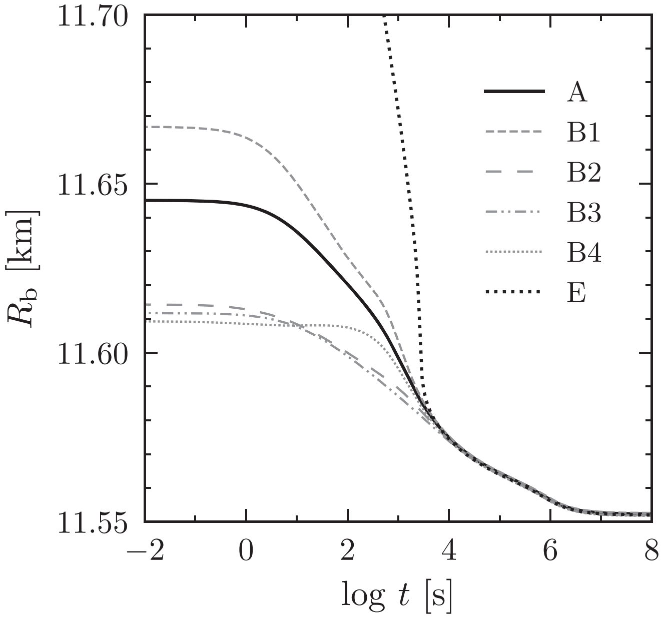

Figure 5. Time evolution of the radius of our 1.4 $M_\odot$ models. See text for details.

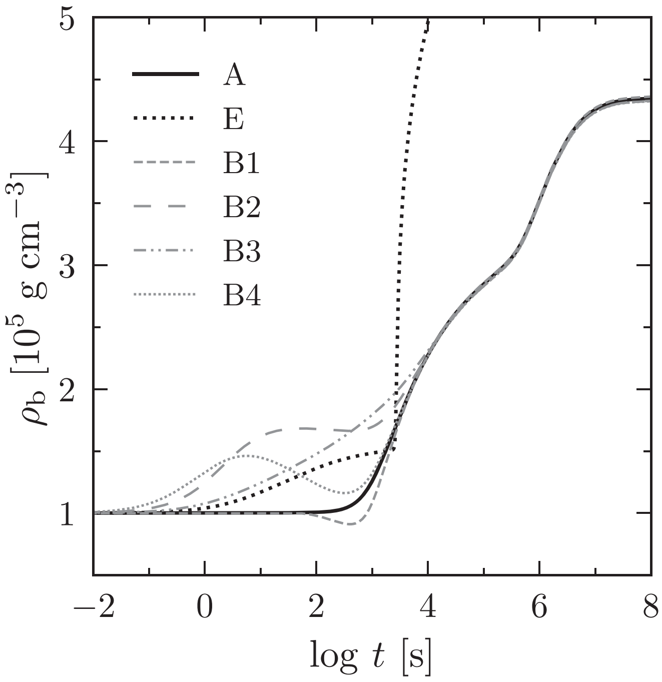

Figure 6. Time evolution of the boundary density ρ_b of our 1.4 $M_\odot$ models. See text for details.

In Figure 5, we show the evolution of the boundary radius R_b of our 1.4 $M_\odot$ models. The different radii at early times are a direct reflection of the inner envelope temperature profiles: hotter envelopes are naturally more expanded. Excluding model E, we find contractions of R_b of the order of 50–100 m. Similarly, in Figure 6, we show the evolution of the outer boundary density ρ_b of the same models. Because ρ_b evolves with T_b in such a way that P_b remains almost constant,[6]

---

[6] There is a small time evolution of P in the outer layers because of contraction, and the resulting small change in g, as seen, e.g., from Equation (13).

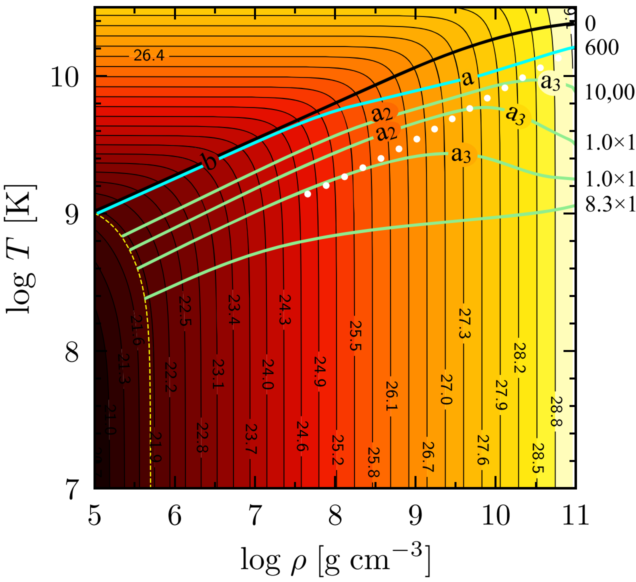

Figure 7. Selected local temperature profiles of model A. Ages, in seconds, are indicated on the right margin. Background color shows the pressure, and contours are isobars labeled with the decimal logarithm of pressure (in dyn cm^{-2}). The dashed (yellow) contour corresponds to the initial P_b and the thick dotted (white) line reproduces the one from Figure 17.

and because T_b is instantaneously correlated with T_eff through the outer envelope, one sees that ρ_b is directly anticorrelated with T_eff as shown in Figure 3(b). On the contrary, R_b results from the integral of the thickness of the underlying layers, and its evolution is not directly correlated with the detailed evolution of ρ_b or T_eff during phase “1.”

Considering, again, our model A in more detail as an illustrative case, we present in Figure 7 a series of envelope temperature profiles. Because we have no mass loss in our models, the column density y_a of any layer is constant during the evolutions and hence each layer evolves at (almost) constant pressure (see footnote 6). We display in the background of Figure 7 the pressure of the medium and a series of isobars: matter evolves along these isobars during the cooling. The profile at 600 s corresponds to the end of the early plateau during which T_eff is locked to $T_\mathrm{eff,Edd}$: we can divide the inner envelope into two regions, layer “a” at densities above $\sim 10^8$ g cm^{-3} where neutrino losses have had a significant effect (compare with Figure 4) and layer “b” below $\sim 10^8$ g cm^{-3} where the temperature profile has almost not evolved. During this phase, R_b has decreased by some 40 m (Figure 5), but this is due to the contraction of layer “a” while layer “b” has not contracted but has rather been slowly sinking, keeping its initial density and temperature profile. After this first phase, T_b and the whole layer “b” are thermally connected to the temperature in layer “a”: T_b, and T_eff, begins to drop following the cooling of “a.” As a result, layer “b” begins to contract and ρ_b begins to increase as exhibited in Figure 6. The evolution of the temperature profile from 600 up to 10^6 s shows a clear difference between the region dominated by pair neutrinos, layer a_2, versus plasmon neutrinos, layer a_3, (separated in the figure by the (white) dotted line). As time runs, layer a_2 encompasses less and less, while layer a_3 encompass more and more, mass. (At these phases, layer “b,” whose energetics is dominated by either Q_V or Q_L, always start at densities around 10^8 as seen in Figure 4.) This different evolution of layers a_2 versus a_3 is easily understood by considering the difference in the temperature dependence of these two neutrino processes (see Figure 17) that results in the strongly different cooling timescales displayed in Figure 18(a). As long as part of the envelope is in the pair neutrino regime, layer a_2 will drive the evolution of the outer layers, and we are in phase “2,” while after $\sim 10^6$, layer a_2 has disappeared, the cooling of the outer layers is driven by layer a_3, and we have entered phase “3.” It is interesting to see in Figure 4 that at age $\sim 10^{5.5}$ s, when the cooling curve passes through the “knee,” the decrease in the pair neutrino emission is so strong that the energetics of layers that were previously dominated by Q_ν are now dominated by Q_L up to densities of $10^{9.5}$ g cm^{-3}.

5.3. Robustness of Our 1.4 $M_\odot$ Star Results

After this thorough study of our model A, let us have a look at models B1 to B4. They are all based on the same two starting points, an interior initially at a temperature $T_0 \simeq 2.5 \times 10^{10}$ K as implied by studies of proto-neutron stars and binary mergers, and a surface luminosity initially at L_Edd, but they have different L and T profiles in -between. These four scenarios have different evolutions only during the early relaxation phase “1” as clearly seen in Figures 3, 5, and 6, a phase where T_eff is driven by the heat diffusion in the low-density part of the inner envelope. However, once the cooling is controlled by neutrino emission, phases “2” and later, their evolutions are identical to scenario A: neutrinos are so efficient that they rapidly erase any remembrance of the initial conditions. Nevertheless, during the first 10^3 s, these different scenarios only span a range of T_eff^∞ between 1.6 and 2.1×10^7 K and a surface luminosity L^∞ between 1 and 3×10^{38} erg s^{-1}. Hence, we have very similar luminosity evolutions during the first half hour and then a basically universal evolution for the first year. Notice that the neutrino processes from either pair annihilation and plasmon decays depend only on the temperature and the electron density and do not depend on the type of nuclei present in the medium. It is only later, during phase “4” controlled by neutrino emission from electron–ion bremsstrahlung, that the actual chemical composition of the medium becomes important.

On the other side, it is well known that the chemical composition of the outer envelope has a strong effect on the T_b–T_s relationship, lighter elements having a larger thermal conductivity and resulting in higher T_s for a given T_b. How large this effect is and how likely are light elements to be present in the high temperature envelope we employ are open questions. Notice that at densities $\sim 10^5$ g cm^{-3} and temperatures $\sim 10^9$ K, thermonuclear rates are enormous and the survival of light elements is doubtful. We intend to tackle these issues in a forthcoming work.

As a distinct initial configuration, let us consider our model F which started with the same $T_{\mathrm{c},0} = 2.5 \times 10^{10}$ K at density $\rho_\mathrm{c} = 10^{11}$ g cm^{-3} but a much lower outer boundary temperature $T_{\mathrm{b},0} \simeq 0.4 \times 10^9$ K at $\rho_\mathrm{b} = 10^5$ g cm^{-3}. This model started with a clearly sub-Eddington L^∞ as seen in Figure 3, but after a few hundred seconds, its surface layers heat up because of the high flux coming from the inner envelope. In Figure 8, we show the temperature profile evolution in the inner envelope: compared to model A, the initial profile has no choice but to have a stronger gradient in the inner part in order to reach a lower $T_{\mathrm{b},0}$, and this is the cause of the rise in T_eff at later times when this enhanced flux reaches the surface. As in

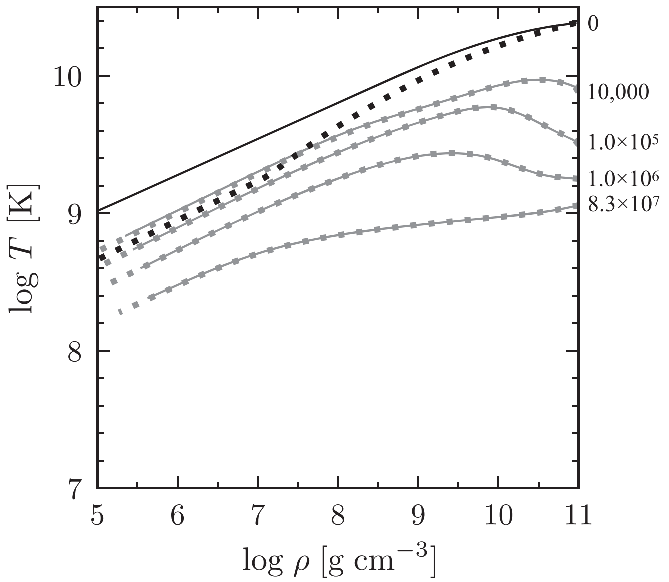

Figure 8. Selected local temperature profiles of model F (dotted lines) compared to model A (solid lines). Ages, in seconds, are indicated on the right margin.

the other models, after $\sim 10^4$ s, the temperature profiles have converged to the universal profiles and are indistinguishable from the ones of model A.

As described in Appendix B, there is some uncertainty regarding the nuclei contribution to the specific heat, but it is only relevant at densities above 10^{10} g cm^{-3} and temperatures well above 10^9 K. This implies that this uncertainty has no effect on the duration of the initial Eddington luminosity phase: this phase terminates when neutrino cooling in region a_2 (see Section 5.2) drives the evolution of $T_{\rm eff}$, and in this region, the nuclei specific heat is negligible.

5.4. Evolution of High- and Low-gravity Stars

In Figure 9, we show the cooling curves for different gravities. Model C with $g_{s,14} \simeq 3.2$ turns out to be very similar to model A with $g_{s,14} \simeq 1.6$: we are plotting the redshifted luminosity, and its intrinsically higher luminosity is in large part compensated by a higher redshift. For the low-gravity models, D and D′, the lower Eddington luminosity clearly shows, and moreover, the relaxation time is much longer: the initial relaxation phase "1" lasts much longer, and an Eddington luminosity can be sustained for more than 10^4 s versus less than 10^3 s for models A and C. Out of curiosity, in model D′, we have arbitrarily switched off the contraction energy of Equation (4): as a result, during the initial relaxation phase, the luminosity slightly decreases instead of staying almost constant as in model D. Nevertheless, at ages between 10^4 up to 10^7 s (i.e., between three hours up to three months), the luminosities of these three models with very different surface gravities are still very similar and only actually differ in details (as, e.g., the time at which the "knee" occurs).

5.5. At the Crossroads of Different Physical Regimes

We finally describe our model E, which has a surface luminosity twice higher than $L_{\rm Edd}$, implying significant mass loss. However, in the inner envelope, the luminosity in this model is still sub-Eddington, due to the fact that the opacity κ is much lower in this region than at the photosphere. We can thus still model the inner envelope within our quasi-static formalism. As seen in Figure 3, this super-Eddington phase can last longer than the Eddington phase of our other models: about 2600 s, after which time $T_{\rm eff}$ suddenly drops.

In Figure 10, we illustrate the evolution of this model through its T profiles. Notice that at early times, the low-density part of the inner envelope is clearly in the radiation-/pair-dominated regime. This regime corresponds in this figure to the

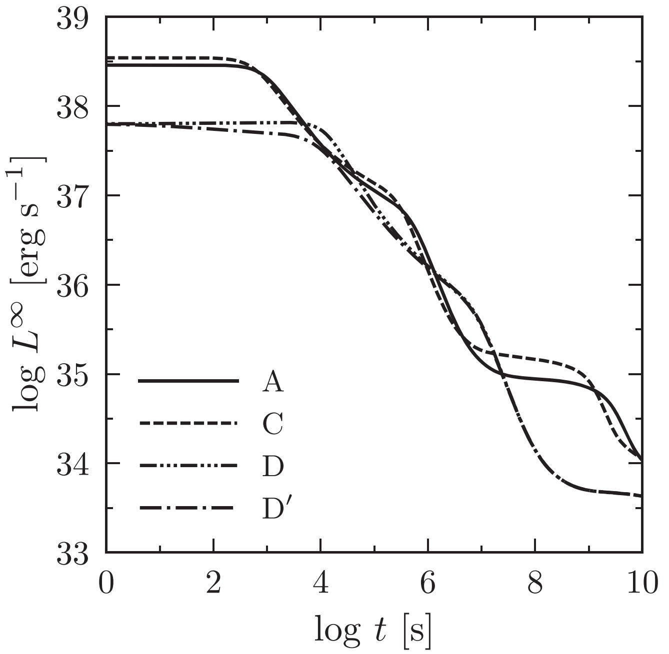

Figure 9. Cooling curves of our models A (1.4 $M_\odot$), C (2 $M_\odot$), D, and D′ (0.25 $M_\odot$). See details in the text.

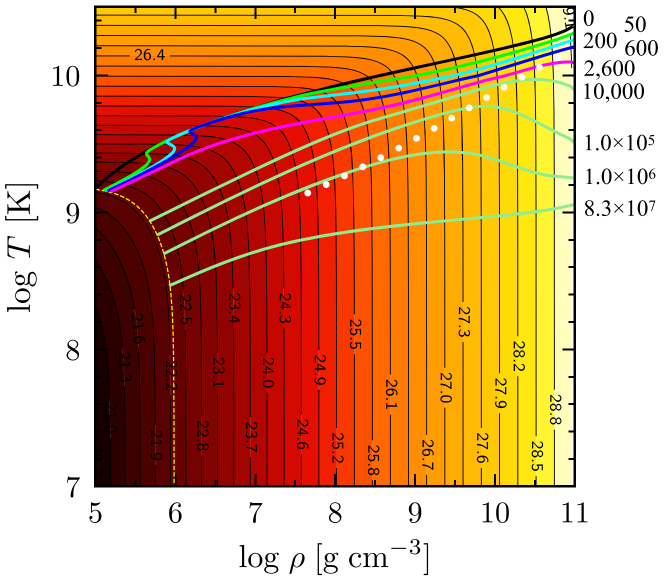

Figure 10. Selected local temperature profiles of model E. Ages, in seconds, are indicated on the right margin. Background color shows the pressure, and the contours are isobars labeled with Log P (dyn cm^{-2}). The dashed (yellow) contour corresponds to the initial $P_{\rm b}$.

region where the isobars are horizontal, i.e., ρ independent, with $P \propto T^4$. In contradistinction, in all our other Eddington luminosity models, the inner envelopes were always in a regime where matter made a strong contribution to the pressure as can be seen, e.g., in Figure 7. This superhot model E results in a strongly puffed-up envelope, because of radiation pressure, as seen from the larger radius R_b in Figure 5. The first four T profiles displayed in Figure 10 show a rapid contraction at the lowest densities. This contraction occurs at (nearly) constant pressure (see footnote 6), hence at (nearly) constant temperature, maintaining a (nearly) constant T_eff, and the gravitational energy released by this contraction is used to power the super-Eddington surface luminosity. This contraction wave propagates inward until it reaches the cooling wave from the neutrino cooling propagating outward from the denser regions. After $\sim$2600 s, further evolution along the isobars implies a significant temperature drop, the inner envelope entering a different pressure regime, and the end of the super-Eddington phase. After $\sim 10^4$ s, this model has forgotten its initial configuration and follows the same evolution as all our other 1.4 $M_\odot$ Eddington luminosity models.

5.6. Effects of a Strong Magnetic Field

Our neo-neutron star study assumes spherical symmetry and ignores the effect of both fast rotation and the presence of a strong magnetic field and is, thus, only a very first step in this direction. Because most realistic scenarios where a neo-neutron star may be observable are likely to produce a fast rotating and strongly magnetized star it is imperative to estimate expected deviations of realistic models from our idealized ones. A simple model intended to mimic fast rotation with a low-gravity model was presented in Section 5.4. The case of a strong magnetic field is more involved as it not only breaks spherical symmetry but introduces strong anisotropies in almost every physical ingredient of our models at both the micro- and macroscopic levels, and modifies the EOS, opacities, thermal conductivities, and also possibly neutrino emission (for reviews about magnetic field effects, we refer the reader to Yakovlev & Kaminker 1994 and Potekhin et al. 2015).

The heat transport anisotropy in the presence of a strong magnetic field and its effects on the thermal emission have been amply studied for a long time in neutron star envelopes (starting from, e.g., Greenstein & Hartke 1983 and Page 1995) and also in deeper layers of the crust (see, e.g., Geppert et al. 2004, 2006 and Pérez-Azorín et al. 2006). The overall effect is that regions of the surface where the magnetic field is tangential to it will be much colder than regions where the field is radial. Due to quantum effects on the thermal conductivity, the hot regions with a radial field are moreover slightly hotter than they would be in the absence of a magnetic field. As a result, when integrating the outcoming flux over the whole stellar surface, one generally obtains luminosities similar to the nonmagnetic case with uniform surface temperature (see, e.g., Page & Sarmiento 1996 for examples with dipolar+quadrupolar magnetic field geometries). We, thus, do not expect that the magnetically induced anisotropy in heat transport results in significant deviations from our results.

A second point of interest is the duration of the early Eddington luminosity phase. It is controlled by neutrino emission from the pair-annihilation process, which occurs at densities above $\sim 10^8$ g cm^{-3}, the layer “a” in Figure 7, and clearly illustrated by the difference between the models A and A$'$ in panel (a) of Figure 3. This process is not affected by the magnetic field at least up to a strength $\sim 10^{14}$ G (Kaminker & Yakovlev 1994). It is only for much stronger fields, which become strongly quantizing even at temperature above 10^{10} K in this density range, that the pair-annihilation process may increase the neutrino losses and reduce the duration of an Eddington phase, but unfortunately, there is no complete calculation available in this density–temperature range to confirm this statement. Synchrotron neutrino emission cannot compete at very high temperatures with the pair-annihilation process, at least for fields below 10^{15} G, and thus is not expected to affect the Eddington luminosity phase for these magnetic field intensities. However, in later phases dominated in the nonmagnetized cases by the plasmon decay process (phase “3” shown in panel (a) of Figure 3), synchrotron neutrinos will increase losses when the field is above $\sim 10^{14}$ G and accelerate the cooling.

The third interesting effect of the presence of a strong magnetic field is the strong suppression of the opacity for extraordinary mode (XO) photons, $\kappa_\mathrm{XO}(\omega) \approx (\omega/\omega_c)^2 \kappa_\mathrm{Th}$ when $\omega \ll \omega_c$, where ω_c is the electron cyclotron frequency and κ_Th the electron-scattering (Thomson) opacity. As a result, when mode switching between the XO and the ordinary (O) mode is taken into account, the critical luminosity L_c (i.e., the Eddington luminosity in the presence of the magnetic field) is increased compared to the zero field L_Edd of Equation (9) by $L_c \approx (\omega_c/\omega) L_\mathrm{Edd}$ and can easily reach 10^{41}–10^{42} erg s^{-1} (Miller 1995). Even higher luminosities, $\sim 10^{44}$ erg s^{-1}, have been observed during magnetar giant flares (see, e.g., Kaspi & Beloborodov 2017), where a hot plasma is likely confined in the magnetosphere (Thompson & Duncan 1995). How long could a strongly magnetized neo-neutron star sustain a high thermal luminosity close to $L_c \sim 10^{41-42}$ erg s^{-1} is the crucial question. In terms of energetics, our model A sustained $L \simeq 3 \times 10^{38}$ erg s^{-1} for about 1000 s and emitted a total of $\sim 3 \times 10^{41}$ erg while our extreme model E kept $L \simeq 6 \times 10^{38}$ erg s^{-1} for about 2500 s, emitting a total of $\sim 2 \times 10^{42}$ erg: this second model had a much hotter and bloated envelope that contained much more energy, both gravitational and thermal, allowing it to sustain a higher luminosity for a long time. Whether a strongly magnetized neo-neutron star envelope will be hot enough and contain sufficient energy to sustain a luminosity close to its possible L_c for a long time (a significant fraction of an hour) is difficult to assess at present time and definitely requires a detailed calculation with all the appropriate physics included. We hope to address this issue in a future paper.

6. Observational Prospects

6.1. Core-collapse Supernova and Supernova Remnants

Neutron stars are great laboratories for studying the EOS of nuclear-density matter. The study of supernova remnants, on the other hand, helps us elucidate the composition and structure of their stellar progenitors (e.g., Lopez et al. 2011). By associating neutron stars with supernova remnants, we can obtain unique information about these systems that is unavailable when we study them separately. What is more, supernova associations provide a way to independently constrain the age of the neutron star as well as searching for former binary surviving companions.

There are, however, clear limitations that prevent us from uncovering young systems, the most noticeable being that the ejecta gas needs to be transparent to the neo-neutron star radiation. For optical (in the absence of dust) and high X-ray energies ($\gtrsim 10\,\mathrm{keV}$), electron scattering provides the main opacity (Bahcall et al. 1970). Let us consider a cloud of gas with mass M_{ej} ejected from the explosion. The cloud radius expands freely as $R = v_{\mathrm{ej}} t$, where $v_{\mathrm{ej}} = \sqrt{2E_{\mathrm{ej}}/M_{\mathrm{ej}}}$ is the characteristic velocity, t is the time since ejection, and E_{ej} is the total kinetic energy. We thus expect an homogeneous envelope to become transparent after a time

$$t_{\tau=1} \approx 0.5 \left(\frac{E_{\mathrm{ej}}}{10^{51}\,\mathrm{erg}}\right)^{-1/2} \left(\frac{M_{\mathrm{ej}}}{5\,M_{\odot}}\right) \mathrm{yr}, \tag{16}$$

which is frustratingly well above the duration of the Eddington luminosity phase. Here we assume $\kappa \approx 0.1\,\mathrm{cm}^2\,\mathrm{g}^{-1}$, which is a reasonable value for ordinary supernova material. At lower X-ray energies ($\epsilon_{\mathrm{x}} \lesssim 3\,\mathrm{keV}$), photoionization may delay the time at which the envelope becomes transparent by an additional factor of $\sim 5(\epsilon_{\mathrm{x}}/1\ \mathrm{keV})^{-3/2}$.

Despite this, the youngest neutron star we have uncovered has an age of about 340 yr (Fesen et al. 2006). In a few instances, a surviving binary companion has been detected in postexplosion deep optical imaging of extragalactic supernova (Maund & Smartt 2009; Folatelli et al. 2014). In the case of 1993J, for example, the brightness of the transient dimmed sufficiently after about a decade so that its spectrum showed the features of a massive star superimposed on the supernova (Maund et al. 2004).

It is perhaps a stinging fact that despite the expected manifestations of neo-neutron stars, one of the main issues in the field has been that most Galactic supernova remnants have no detectable central source. Figure 11 shows the current detections and upper limits of thermal emission in nearby neutron stars with model predictions. Observational selection effects are clearly at play when uncovering young objects yet there is the possibility that a sizable fraction of massive star collapses might produce black holes rather than neutron stars, with the clearest example being W49B (Lopez et al. 2013) and the other four examples, from Kaplan et al. (2004, 2006), all plotted in Figure 11.

6.2. Neutron Star Mergers, Short Gamma-Ray Bursts, and LIGO Events

The merger of binary neutron stars and the subsequent production of a beamed, relativistic outflow are believed to trigger short gamma-ray bursts (e.g., Abbott et al. 2017a) and expel metallic, radioactive debris referred to as a kilonova (e.g., Kasen et al. 2017). The ultimate fate of the postmerger remnant remains unclear and is dependent on the mass limit for the support of a hot, differentially rotating neutron star. The merged remnant can either collapse and form a low-mass black hole (Eichler et al. 1989; Rezzolla et al. 2011; Murguia-Berthier et al. 2014) or survive as a hypermassive neutron star (Usov 1992; Kluźniak & Ruderman 1998; Metzger et al. 2008, 2018). In that case, the detectability of the hypermassive remnant will depend primarily on the orientation of the merging binary.

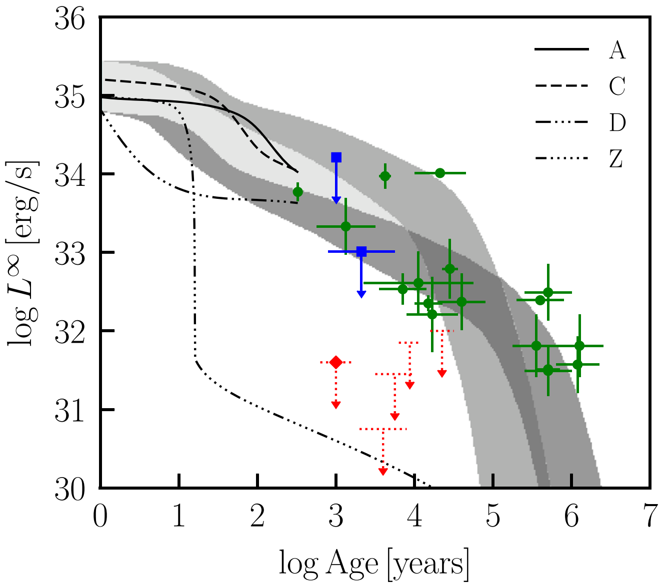

Figure 11. Plot of luminosity as a function of the age of the remnant for nearby neutron stars together with the predictions from neutron star cooling models. The (green) dots are measurements and the (blue) squares are upper limits from detected neutron stars (data taken from Beznogov & Yakovlev 2015) while the (red) dotted error bars are upper limits on the compact objects, black holes or neutron stars, expected to be presents in five core-collapse supernova remnants. These remnants are, in order of increasing age: G043.3–0.2 (a.k.a. W49B, marked by a diamond) from Lopez et al. (2013), and G127.1+0.5, G084.2+0.8, G074.0–8.5, and G065.3+5.7 from Kaplan et al. (2004, 2006). Shaded areas show model predictions of Page et al. (2004, 2009) for the minimal cooling of neutron stars that cover uncertainties on the chemical composition of the envelope and nucleon pairing at high densities. In contradistinction, the dashed-pentadotted curve, Z, exemplifies the effect of fast neutrino emission from the direct Urca process expected to occur in massive neutron stars (Boguta 1981; Lattimer et al. 1991) resulting in very cold stars (Page & Applegate 1992). Also plotted are the three different models (A, C, D) shown in Figure 9.

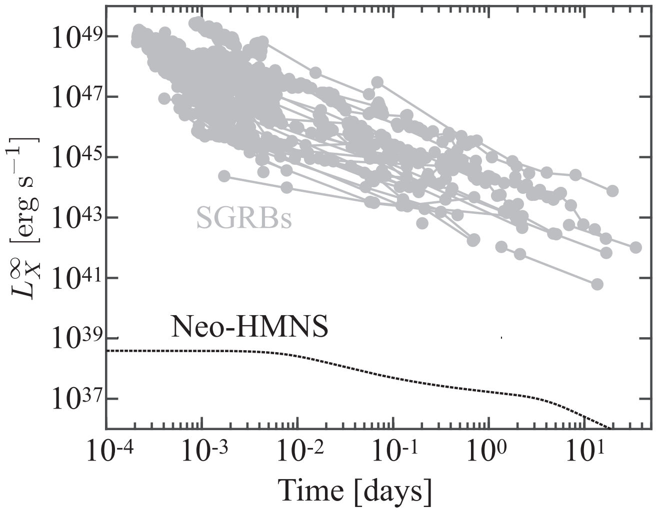

Figure 12. Plot of the on-axis X-ray afterglow light curves from a sample of 36 short GRBs with well-sampled light curves and redshifts compiled by Fong et al. (2017). Also plotted is the X-ray luminosity of the cooling model C shown in Figure 3, labeled as a hypermassive neutron star (HMNS).

When the relativistic jet points in the direction of the observer, the event will likely be detected as a classical short gamma-ray burst (Lee & Ramirez-Ruiz 2007; Nakar 2007) and the X-ray emission emanating from the surviving remnant will be buried by the luminous afterglow emission. This can be seen in Figure 12, where we compare the X-ray luminosity of the cooling model C shown in Figure 9 to the on-axis X-ray afterglow luminosities of a sample of short gamma-ray bursts.

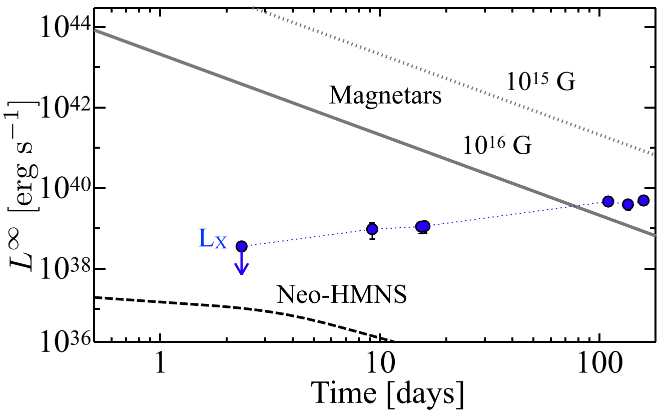

Figure 13. Plot of the X-ray light curves of the counterpart to GW170817 from *Chandra* (0.3–10 keV) and cooling model C shown in Figure 3 (labeled Neo-HMNS). Also plotted, for comparison, are the spin-down (bolometric) luminosities expected for a stable hypermassive magnetar. Adapted from Margutti et al. (2018).

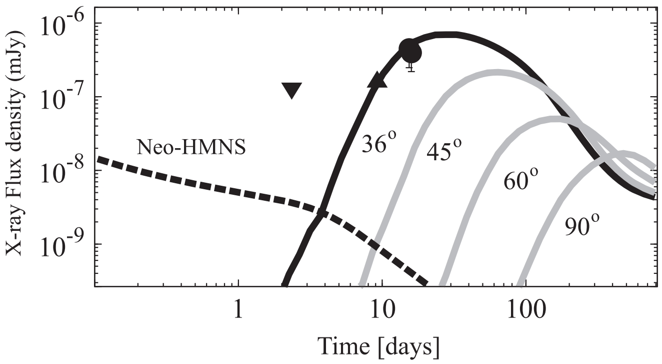

Figure 14. Plot of the X-ray flux density at 1 keV for an off-axis model with 10^{49} erg and $\theta_{\rm obs} = 36°$ from Margutti et al. (2017) aimed at providing a reasonable description of the X-ray data of GW170817. Also shown are the corresponding models for observers seeing the same event but farther away from the axis of the jet and the cooling model C (labeled Neo-HMNS).

Our ability to directly uncover the emission of the newly formed, hypermassive neutron star drastically increases when the event is off axis, as was the case for GW170817 (Abbott et al. 2017a, 2017b). In 2017 August, Coulter et al. (2017) discovered the first optical counterpart to a gravitational wave source, in this case, the cataclysmic merger of two neutron stars. This landmark discovery initiated the field of gravitational wave astronomy and enabled an exhaustive observational campaign (Abbott et al. 2017b). In Figure 13, we show the luminosity of the X-ray counterpart to GW170817 (Margutti et al. 2018) that is seen to be significantly dimmer than the one expected from the spin down of a highly magnetized, rapidly rotating remnant but only slightly brighter than the X-ray luminosity predicted for the relevant cooling model C that is plotted in Figure 9.

The constraints imposed by the afterglow observations favor the idea that GW170817 was a typical GRB jet seen off axis (Abbott et al. 2017a, 2017b). This interpretation assumes that our line of sight is tens of degrees from the core of the jet and thus suggests that the prospects for detecting the remnant directly might be doable for future events, in particular if they are seen farther away from the axis of the jet as can be seen in Figure 14.

As discussed in the case of core-collapse supernovae, one of the challenges for direct detection is that the neo-neutron star is likely to be surrounded by a thick and expanding radioactive ejecta. In the case of GW170817, the optical depth is expected to be dominated by the *r*-process, radioactively powered, kilonova ejecta (e.g., Metzger et al. 2010; Roberts et al. 2011; Kasen et al. 2017). Given the quantities derived for the neutron star merger outflow of GW170817 (e.g., Kasen et al. 2017; Kilpatrick et al. 2017; Murguia-Berthier et al. 2017; Villar et al. 2017; Ramirez-Ruiz et al. 2019), we expect the ejecta to become transparent after a time

$$t_{\tau=1} \approx 1.1 \left(\frac{E_{\rm ej}}{10^{50}\,{\rm erg}}\right)^{-1/2} \left(\frac{M_{\rm ej}}{10^{-2}\,M_\odot}\right) {\rm days}, \tag{17}$$

where we have used $\kappa \approx 10\,{\rm cm}^2\,{\rm g}^{-1}$ for the much more opaque *r*-process rich ejecta (Barnes & Kasen 2013). Given the low-mass ejecta, double neutron star mergers appear to be a viable system for uncovering a neo-neutron star, provided that the surviving remnant is stable. Alternatively, the lack of X-ray detection of the cooling signal could be used to argue in support of a collapse to a black hole.

6.3. Neo-neutron Stars in Accretion-induced Collapse Events

Another relevant progenitor avenue for our study is the formation of a neutron star through the collapse of oxygen–neon white dwarf stars in interacting binaries (Canal & Schatzman 1976; Miyaji et al. 1980; Canal et al. 1990; Nomoto & Kondo 1991; Wang 2018a). An oxygen–neon white dwarf in a binary system might be able to augment its mass near the Chandrasekhar mass, leading to accretion-induced collapse by accreting steadily or dynamically (e.g., Wang 2018b; Ruiter et al. 2019). The formation of neutron stars from interacting oxygen–neon white dwarfs in binaries is likely to be accompanied by low-mass ejecta (Woosley & Baron 1992; Dessart et al. 2006; Metzger et al. 2009; Darbha et al. 2010), which might help direct detection.

The prospects for detection of the predicted transients appear promising (Darbha et al. 2010), yet their characterization might be difficult as they might be confused with other thermal transients predicted to occur on similar timescales (≈few days) such as failed deflagrations (Livne et al. 2005) and Type .Ia supernovae (Bildsten et al. 2007). Such events are, however, not expected to be accompanied by an X-ray transient. For an ejecta mass of $M_{\rm ej} = 10^{-2}\,M_\odot$, we expect these optical transients to be uncovered by upcoming surveys to distances of a few 100 Mpc (Darbha et al. 2010), which will make the X-ray characterization of the neo-neutron star doable with current space-based facilities.

7. Summary of Results and Conclusions

We have presented a detailed study of the evolution of the outer layers of a neo-neutron star. We started just after the end of the proto-neutron star phase when the internal temperature has dropped to $\sim 2.5 \times 10^{10}$ K at densities $\sim 10^{11}$ g cm^{-3} and above. At these temperatures, the nuclei in the crust have already been formed. We developed a model of the outer envelope, i.e., the region from the photosphere up to densities around $\sim 10^{5-6}$ g cm^{-3}, at luminosities close to the Eddington luminosity, in stationary state, presented in Figure 1. Using an extension of the neutron star cooling code `NSCool` (Page 1989, 2016), we then modeled the whole neutron star, but focused on the description of the evolution of the inner envelope, at densities between 10^5 and 10^{11} g cm^{-3}. The evolution of the surface temperature, and hence the star's surface thermal luminosity, during this early neo-neutron star phase in controlled by the evolution of the inner envelope and is thermally decoupled from the deeper layers on such short timescales. The initial condition of temperature $\sim 2.5 \times 10^{10}$ K at high densities and surface Eddington luminosity leave some, but not much, space for variability of the temperature and luminosity in the inner envelope as shown in Figure 2. As a result, the surface luminosity remains close to the Eddington value, i.e., above 10^{38} erg s^{-1}, for a few thousand seconds with effective temperatures of the order of 1.5–2 $\times$ 10^7 K, as presented in Figure 3 for a 1.4 $M_\odot$ star. After $\sim 10^3$ s, the surface temperature evolution is controlled by neutrino emission, initially by pair annihilation in the inner envelope for some 10^5 s followed by plasmon decay until it has decreased to a few million Kelvin and reached the "early plateau," well known from isolated neutron star cooling theory. Models with either larger or lower surface gravity have an initially different Eddington luminosity but later follow a very similar cooling trajectory during their first year of evolution, as illustrated in Figure 9. At ages between 10^4 and 10^7 s, the luminosity drop is roughly, within a factor of a few, a power law,

$$L(t) \simeq 3 \times 10^{37} (t/10^4 \mathrm{s})^{-3/4} \ \mathrm{erg\ s^{-1}}. \tag{18}$$

Neutron stars in the universe could have very different origins, including core-collapse supernovae, neutron star mergers, white dwarf collapses, and the so-called electron-capture supernovae that are somewhat similar to the accretion-induced collapse. In the case of birth in a core-collapse supernova, it is very unlikely that the neo-neutron star could be observed as it takes at least a few months until the remnant could become transparent to soft X-rays. In the case of SN 1987A, it was only after more than 30 yr that the first signal of the existence of a neutron star was possibly observed (Cigan et al. 2019). However, in the case of a born-again neo-neutron star produced by the merging of two neutron stars, as is expected to be the case in short GRBs and in the GW170817 event, the chances of detecting the neo-neutron star are encouraging. If the merger produces a GRB and we are strongly off axis, the neo-neutron star could be detectable once the kilonova ejecta have sufficiently expanded to become transparent to soft X-rays, which should take about a day (see Equation (17)). In the case of accretion-induced collapse of a white dwarf, the situation is similar with little ejected material.

The direct detection of a neo-neutron star can thus be aided if the formation is followed by the ejection of low-mass ejecta as in the case of neutron star mergers and accretion-induced collapses of white dwarfs. Interestingly, in both scenarios, the neo-neutron star is expected to be rapidly rotating, and if it has a sufficiently high magnetic field, then the spin-down luminosity might prevent the detection of the cooling signature (Rosswog et al. 2003; Price & Rosswog 2006). Our understanding of neutron star birth has come a long way since the pioneering work by Baade & Zwicky (1934) more than eight decades ago, but these enigmatic sources continue to remain elusive, in particular at very young ages. Neutron star mergers and accretion-induced collapses of white dwarfs provide us with an exciting opportunity to study new regimes of physics and to learn what these systems were like at the earliest epochs of formation when their luminosities are near the Eddington limit. Electromagnetic and gravitational wave observatories over the coming years offer the potential to uncover the detailed nature of these most remarkable objects.

M.B. and D.P. are partially supported by the Consejo Nacional de Ciencia y Tecnología with a CB-2014-1 grant #240512. M.B. also acknowledges support from a postdoctoral fellowship from UNAM-DGAPA. The first steps of this work were financed by a UNAM-DGAPA grant #113211. E.R.-R. acknowledges support from the Heising-Simons Foundation, the Danish National Research Foundation (DNRF132), and NSF (AST-1911206). The authors thank A. Raduta for some guidance about the nuclei specific heat and J. Schwab, R. Foley, and L. Lopez for illuminating discussions.

Software: NSCool (Page 1989, 2016).[7]

Appendix A
Physical State of Matter in the Inner Envelope

As discussed in Section 4 in the inner envelope we are dealing with matter at densities $\rho_\mathrm{b} = 10^5 < \rho < \rho_\mathrm{c} = 10^{11}$ g cm^{-3} and temperatures $(1\text{–}3) \times 10^9 < T < (1\text{–}3) \times 10^{10}$ K. At these temperatures and densities, one has to take into account the presence of positrons and photons. Below we briefly describe the physical ingredients employed in our model and present illustrative plots that allow us to better understand our results.

A.1. Equation of State

We assume the presence of ^{80}Ni at ρ_c (following Haensel et al. 1989) and ^{56}Fe at ρ_b, while we interpolate in both A and Z linearly in $\log \rho$ at intermediate densities. Pressure is obtained as the sum of radiation, free gases of electrons and positrons, and a free gas of nuclei plus Coulomb interaction corrections following Potekhin & Chabrier (2010). Crystallization of ions takes place when the Coulomb coupling parameter $\Gamma \equiv (Ze)^2/(a_\mathrm{WS} k_\mathrm{B} T)$ reaches 175 ($a_\mathrm{WS} = (4\pi n_\mathrm{i}/3)^{-1/3}$ is the Wigner–Seitz cell radius, n_i being the number density of ions and Ze their electric charge).

A.2. Opacity and Thermal Conductivity

The thermal conductivity K is taken as the sum of the electron, K_e, and photon, K_ph, conductivities. In the inner envelope, the plasma is fully ionized. Thus, there is no need to take into account the effects of partial ionization on opacity. The radiative opacity κ_rad consists of two terms: free–free absorption and electron scattering. The former was calculated based on the fits of Schatz et al. (1999). The latter is based on the modern fit of Poutanen (2017), which takes into account electron degeneracy and pair production (the fit handles both Thompson and Compton scattering). A correction factor of Potekhin & Yakovlev (2001) was used for adding free–free and electron-scattering opacities. The electron thermal conductivity is taken from Yakovlev & Urpin (1980) when ions are in a liquid phase and from Potekhin et al. (1999) in the solid phase.

The resulting thermal conductivity K is illustrated in Figure 15 as well as the corresponding total opacity κ defined by

$$\kappa = \frac{4acT^3}{3K\rho}. \tag{19}$$

---

[7] The version of the code used in the paper is not publicly available at the present time, but the modifications are described in Appendix C.

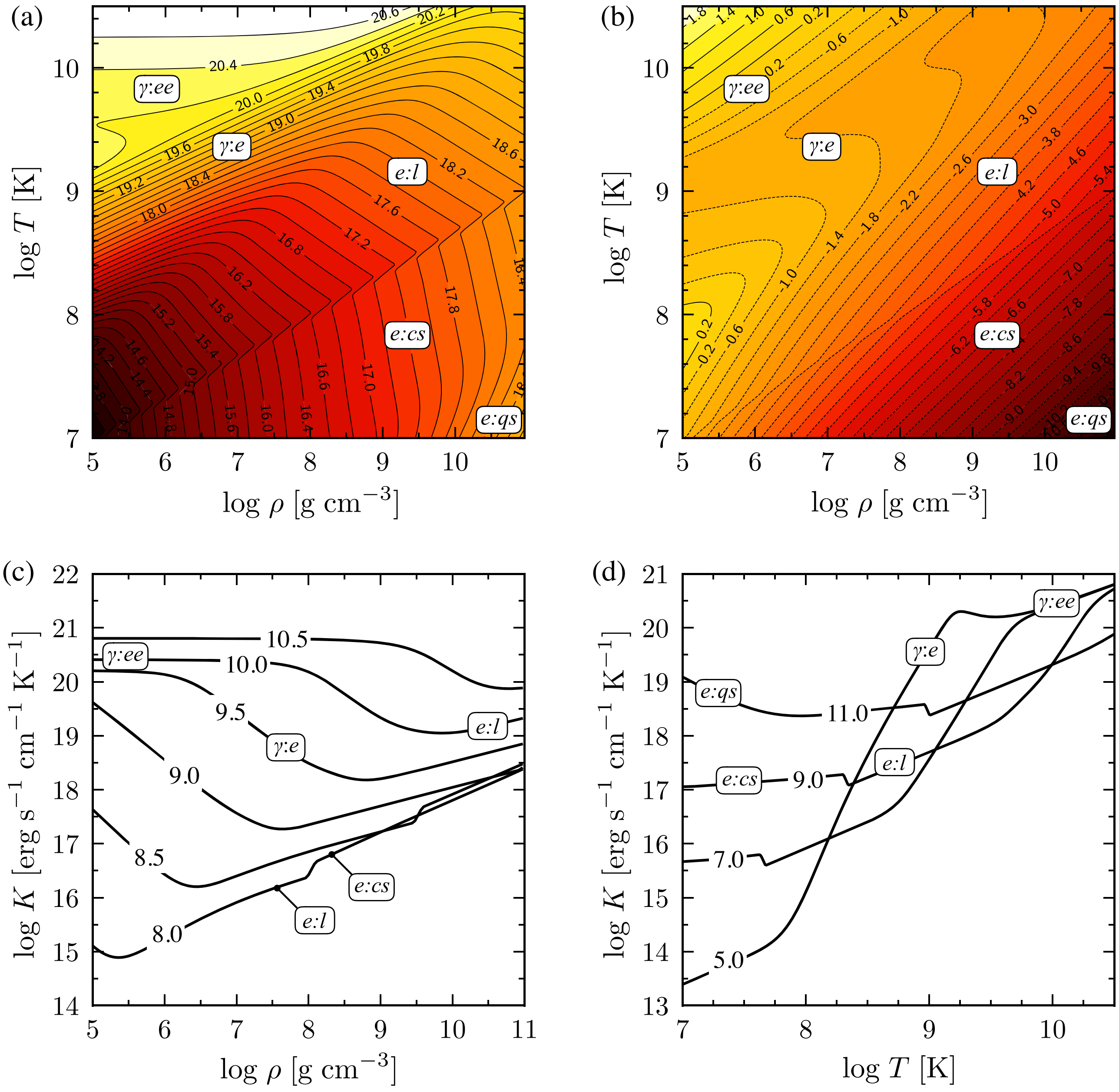

Figure 15. Thermal conductivity K and total opacity κ for the conditions of the inner envelope. Panel (a) shows the contour plot of conductivity, panel (b) of opacity (from Equation (19)), panels (c) and (d) demonstrate the thermal conductivity as a function of density, for a constant temperature; and temperature, for a constant density, respectively. Values on the contour lines in panel (a) are decimal logarithms of the conductivity (in erg s^{-1} cm^{-1} K^{-1}), in panel (b) decimal logarithms of opacity (in cm^2 g^{-1}), on curves in panel (c) are decimal logarithms of temperature (in Kelvin), and values on curves in panel (d) are decimal logarithms of density (in g cm^{-3}). The boxed labels in panels (a) and (b) indicate the dominant contribution to the thermal conductivity for a given temperature and density region, as described in the text, and a few of them are reproduced in the other two panels.

This κ, which includes contributions from photons and electrons, should not be confused with the more restricted (Rosseland mean) radiative opacity.

The different shapes of the contour lines in panel (a) clearly exhibit different regimes that are indicated by the boxed labels:

1. γ: *ee*—conductivity dominated by photons and controlled by Thomson/Compton scattering on electrons and positrons;
2. γ: *e*—conductivity dominated by photons and controlled by Thomson scattering on electrons;
3. *e*: *l*—conductivity dominated by electrons and controlled by scattering on ions in the liquid phase;
4. *e*: *cs*—conductivity dominated by electrons and controlled by scattering on ions in a classical Coulomb solid;
5. *e*: *qs*—conductivity dominated by electrons and controlled by scattering on ions in a quantum Coulomb solid.

In the density regime considered here for the inner envelope, photon opacity is dominated by free–free absorption only in a very narrow region at the transition between photon-dominated to electron-dominated transport. We have a discontinuity in the electron conductivity along the melting curve, which may be fictitious as argued by Baiko et al. (1998) but which is small enough and occurring at densities high enough that it has a negligible effect on our results. Notice the dramatic effect of

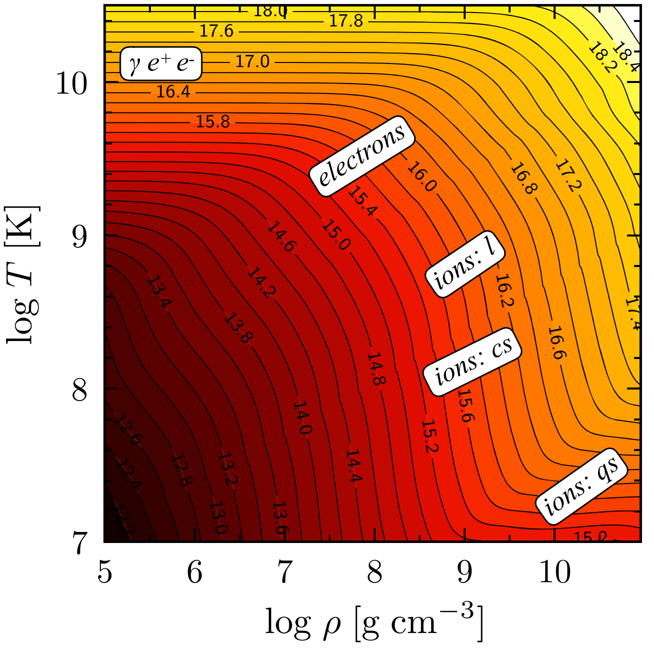

Figure 16. Specific heat for the conditions of the inner envelope. Values on the contour lines are decimal logarithms of the specific heat capacity (in erg cm^{-3} K^{-1}). Boxed labels indicate the dominant contributor in the various temperature and density regions. See details in the text.

pairs in limiting K at high temperatures simply due to the strong increase in the number of scatterers, electrons and positrons, with temperature in this regime.

A.3. Specific Heat

The specific heat is computed as described in Potekhin & Chabrier (2010) to which we added the contribution of radiation and pairs when present. As we are interested in temperatures up to about 1–2 MeV, we have moreover added the contribution of nuclear excitations as discussed in Appendix B.

Contour plots of the total specific heat are shown on Figure 16. The different regimes, as indicated by the boxed labels are:

1. $\gamma\ e^+\ e^-$—photons and electron–positron pairs;
2. *electrons*—electrons;
3. *ions*: *l*—ions in a Coulomb liquid;
4. *ions*: *cs*—ions in a classical Coulomb solid;
5. *ions*: *qs*—ions in a quantum Coulomb solid.

Nuclear excitation never dominates but makes a significant contribution at the highest densities ($\gtrsim 10^{10}$ g cm^{-3}) and temperatures ($\gg 10^9$ K).

A.4. Neutrino Emission

In the density range of our inner envelope, $10^5 - 10^{11}$g cm^{-3}, neutrino emission is dominated by three process, in order of decreasing temperature importance: e^+–e^--pair annihilation, plasmon decay, and e-ion bremsstrahlung. For the first two, we follow Itoh et al. (1996), and Kaminker et al. (1999) for the third one. We present in Figure 17 contour plots of the total neutrino emissivity. Notice the dramatic change in temperature dependence when crossing the (dotted white) line from pair annihilation to plasmon decay dominance. The very strong temperature dependence of the pair-annihilation process when approaching this line is due to the exponential suppression of pairs when electrons become degenerate. Similarly, when shifting from plasmon decay to electron–ion bremsstrahlung, the temperature dependence of the plasmon process increases rapidly due to the exponential suppression of plasmons below the plasmon temperature.

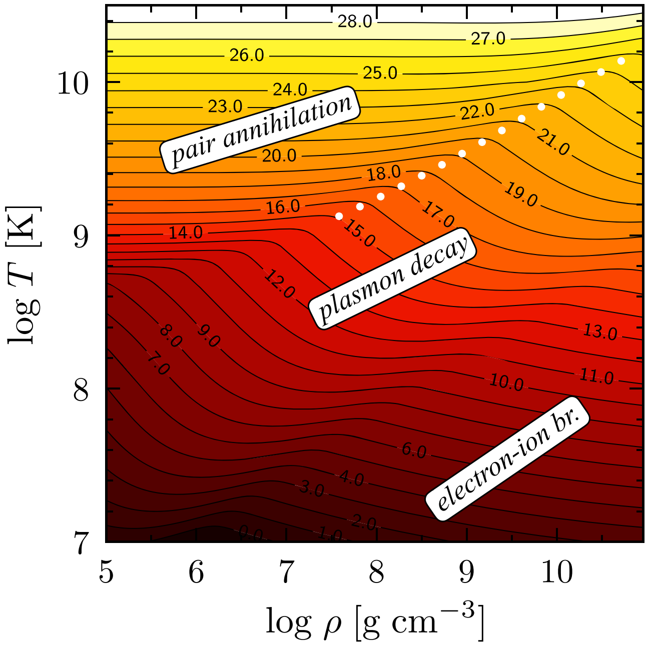

Figure 17. Neutrino emissivity for the conditions of the inner envelope. Values on the contour lines are decimal logarithms of the neutrino emissivity (in erg cm^{-3} s^{-1}). Boxed labels indicate the dominant process in the various temperature and density regions (where "electron–ion br." stands for electron–ion bremsstrahlung), and the thick dotted (white) line explicitly marks the transition from pair annihilation to plasmon decay for later reference (the line is not shown at low densities because neutrino losses become negligible in this regime). See details in the text.

A.5. Timescales

Besides the microphysics ingredients, κ, C_V, and Q_ν, the two evolutionary timescales dictated by them are also very illustrative: the neutrino cooling timescale $\tau_\nu \equiv C_V/Q_\nu$ and the heat diffusion timescale $\tau_\mathrm{h} \equiv C_V/K$. We display both of them in Figure 18 as they are very helpful to understand our results.

Appendix B
Nuclei Specific Heat

In principle, the calculation of specific heat is straightforward as it can be directly derived from the system's partition function $Z = Z(T)$ (see, e.g., Landau & Lifshitz 1993) as

$$C_V = k_\mathrm{B} T \left(2\frac{Z'}{Z} - T\left(\frac{Z'}{Z}\right)^2 + T\frac{Z''}{Z}\right), \tag{20}$$

where the primes denote derivative with respect to the temperature T, and k_B is the Boltzman constant. We describe below how we proceeded to calculate the partition function.

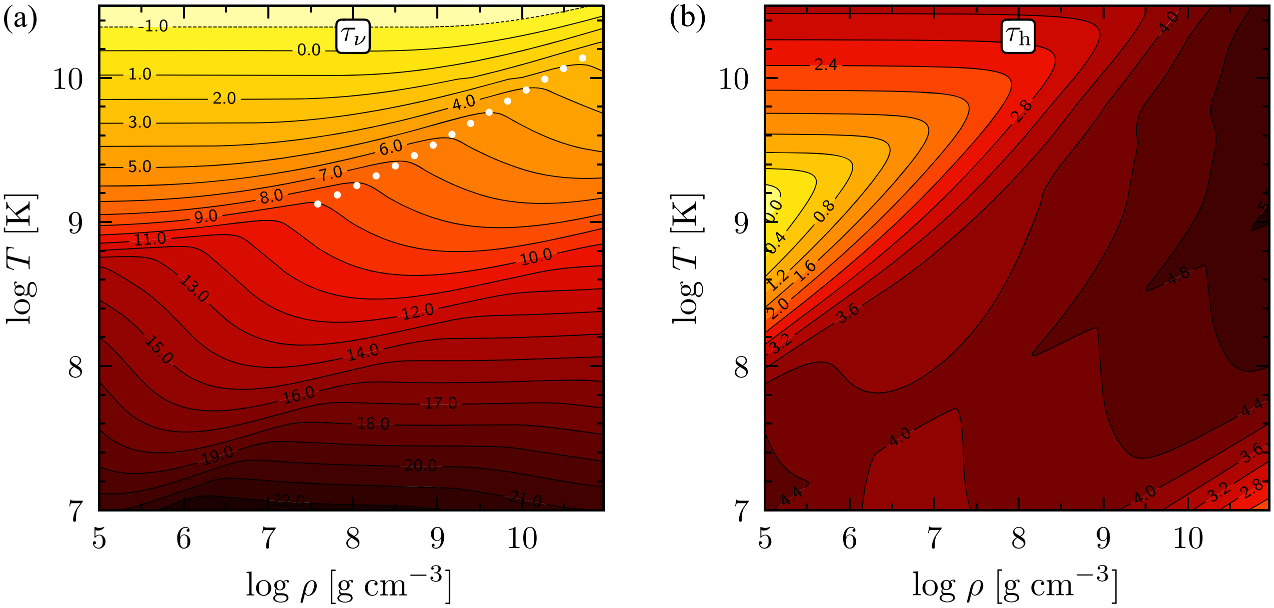

Figure 18. Timescales in the inner envelope. Panel (a) shows contours of the neutrino cooling timescale $\tau_\nu \equiv C_V/Q_\nu$, the curve labels giving the decimal logarithms of τ_ν in units of second per GK (because 10^9 K is a typical temperature in our neo-neutron star envelopes). The thick dotted (white) line reproduces the one from Figure 17. Panel (b) shows contours of the heat diffusion timescale $\tau_\mathrm{h} \equiv C_V/K$, the curve labels giving the decimal logarithms of τ_h in units of second per $(10\ \mathrm{m})^2$ (because 10 m is a typical length scale in our neo-neutron star envelopes).

The nucleus has a discrete excitation energy spectrum but only low-lying energy levels (up to a few MeV) are known reliably from experiments. Moreover, at higher energies, the density of states grows so rapidly that it is more convenient to approximate with a continuous distribution. If $\rho_\mathrm{LD}(E, J)$ is the density of energy levels of angular momentum J at energy E, the "observable level density" is $\rho_\mathrm{LD}(E) = \sum_J \rho_\mathrm{LD}(E, J)$ while the density of states or "true level density," which takes into account the spin degeneracy, is $\Omega_\mathrm{DS}(E) = \sum_J (2J + 1)\, \rho_\mathrm{LD}(E, J)$ (Gilbert & Cameron 1965; Huizenga & Moretto 1972). We will follow the commonly used Back-Shifted Fermi Gas (BSFG) approximation (see, e.g., von Egidy & Bucurescu 2005), an extension of the noninteractive Fermi gas model of Bethe (1936), in which

$$\Omega_\mathrm{DS}(E) = \frac{\sqrt{\pi}\, \exp\left(2\sqrt{a(E - E_1)}\right)}{12\, a^{1/4}(E - E_1)^{5/4}} = \sqrt{2\pi}\,\sigma\, \rho_\mathrm{LD}(E) \qquad (21)$$

where E_1 is the energy backshift, a the level density parameter, and σ the spin cutoff, whose values are obtained by fitting experimental data. Within this approximation, we can calculate $Z(T)$ as

$$Z(T) = \sum_{i=0}^{i=i_\mathrm{cf}} g_i \exp\left(-\frac{E_i}{k_\mathrm{B} T}\right) + \int_{E_\mathrm{cf}}^{\infty} \Omega_\mathrm{DS}(E) \exp\left(-\frac{E}{k_\mathrm{B} T}\right) dE \qquad (22)$$

where $E_\mathrm{cf} = E_{i_\mathrm{cf}}$ is some arbitrary energy cutoff level to switch from discrete to continuous regime; g_i is the spin degeneracy factor, which is obtained experimentally together with the energy levels E_i. In the continuous spectrum range, the spin degeneracy is in principle taken into account in $\Omega_\mathrm{DS}(E)$. This spin degeneracy is not experimentally determined in the high-excitation (continuous) regime, and there are large uncertainties in its value (see, e.g., von Egidy & Bucurescu 2009) and for this reason many authors prefer to use $\rho_\mathrm{LD}(E)$ instead of $\Omega_\mathrm{DS}(E)$ in the evaluation of $Z(T)$ in Equation (22).

We used the procedure described above to calculate the contributions of ^{56}Fe and ^{60}Ni nuclei to the heat capacity. For ^{56}Fe, we used experimental data on the energy levels and spin degeneracy factors from Junde et al. (2011) and for ^{60}Ni—from Browne & Tuli (2013).[8] The values of E_1 and a were taken from the recent fits of Bucurescu & von Egidy (2015). The choice of the cutoff energy is important, so we tried two approaches: cutoff at 5 MeV and cutoff at the first energy level for which the experimental value of g is not known. In the latter case, the cutoff energy was ~3.8 MeV for ^{56}Fe and ~3.3 MeV for ^{60}Ni. The heat capacity calculated using Equations (20), (21), and (22) is per nucleus. Thus, one has to multiply it by the ion number density $n_\mathrm{i} = \rho/(A m_u)$, where A is the nucleus atomic mass number and m_u is the atomic mass unit. The results are presented in Figure 19, which shows the heat capacity of both the nuclei and the total, as a function of temperature at two fixed densities $\rho = 10^{10}$ and 10^{11} g cm^{-3}. The solid black curve corresponds to ^{56}Fe, dashed black curve to ^{60}Ni, dotted–dashed black curve to the total heat capacity including contribution from ^{56}Fe nuclei, and dotted–dashed gray curve to the total heat capacity excluding nuclei contribution. The solid gray curve demonstrates the ^{60}Ni nuclei heat capacity for the energy cutoff of 5 MeV instead of ~3.3 MeV (see previous paragraph). The dashed gray curve shows the ^{60}Ni nuclei heat capacity calculated employing the level density ρ_LD instead of the density of states Ω_DS in Equation (22).

From Figure 19, one can draw several conclusions. First, at low temperatures ($T \sim 10^9$ K), the ^{56}Fe and ^{60}Ni heat capacities are considerably different. This is not a surprise because at these temperatures, the heat capacity is governed by the first few low-lying energy levels, which can differ rather

---

[8] All data are available online at http://www.nndc.bnl.gov/chart/.

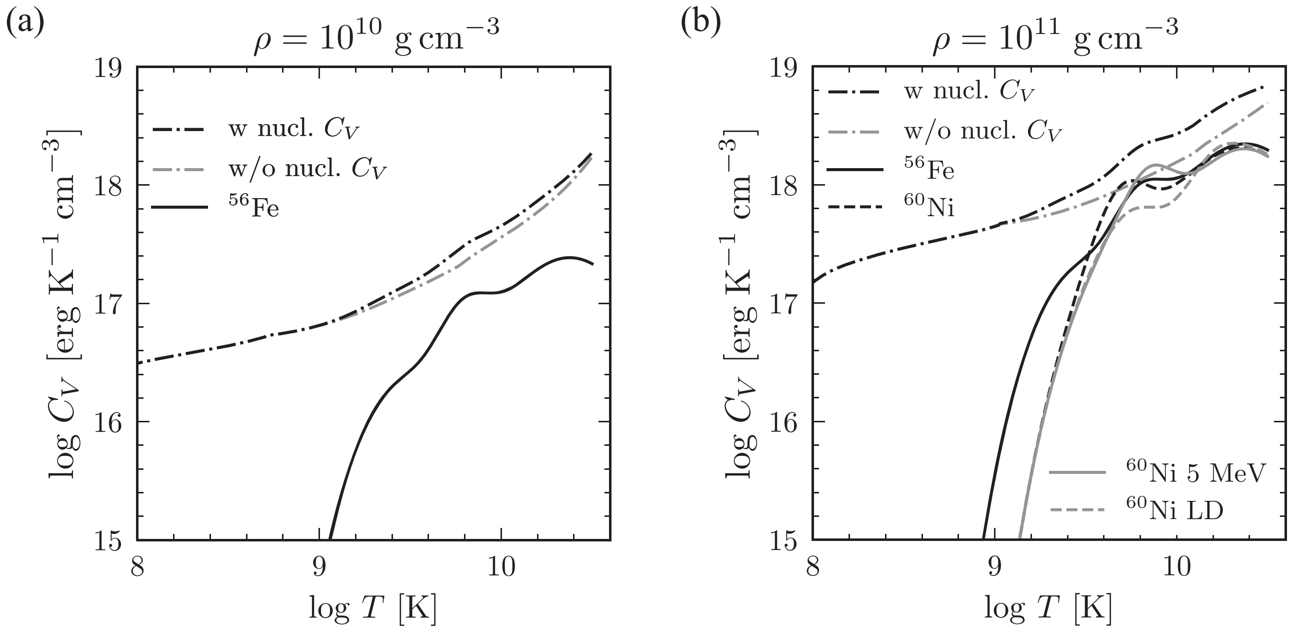

Figure 19. Heat capacity, of both the nuclei and the total, as a function of temperature at two fixed densities $\rho = 10^{10}$, panel (a), and 10^{11} g cm^{-3}, panel (b). The solid black curve corresponds to ^{56}Fe, dashed black curve to ^{60}Ni, dotted–dashed black curve to the total heat capacity including contribution from ^{56}Fe nuclei, and dotted–dashed gray curve to the total heat capacity excluding nuclei contribution. The solid gray curve demonstrates the ^{60}Ni nuclei heat capacity for the energy cutoff of 5 MeV. The dashed gray curve shows the ^{60}Ni nuclei heat capacity calculated employing the level density $\rho_{\rm LD}$ instead of the density of states $\Omega_{\rm DS}$. See details in the text.

noticeably even for similar nuclei. On the other hand, this does not matter much as at $T \sim 10^9$ K, nuclei heat capacity is much less than the total heat capacity and, thus, can be ignored. Second, the maximum contribution of the nuclei heat capacity to the total heat capacity is achieved at $T \sim 10^{9.8}$ K and can be around 50% of the total heat capacity at $\rho = 10^{11}$ g cm^{-3}. Nuclei heat capacity is directly proportional to the density of matter (see paragraph before previous), thus, its contribution at lower densities is lower and at sufficiently low densities ($\rho \lesssim 10^9$ g cm^{-3}) can be ignored at any temperature. Third, at temperatures $T \sim 10^{9.6}$–10^{10} K, nuclei heat capacity is sensitive to the particular nuclear species and to the choice of the energy cutoff. The difference can be up to ~2 times. At higher densities, one enters the neutron drip regime where the heat capacity is dominated by the dripped neutron liquid (see e.g., Page & Reddy 2012) and the contribution from the nuclear excitations can again be ignored.

Appendix C
Numerical Method

We base our calculations on the code `NSCool` (Page 1989, 2016) with important adjustments to solve for hydrostatic equilibrium in the inner envelope in the conditions where the radiation and pair pressures are important.

The structure equations are initially solved from the center of the star down to $\rho_{\rm c} = 10^{11}$ g cm^{-3} employing the zero-temperature EOS, and this interior structure is not modified afterward. At densities between $\rho_{\rm c}$ and $\rho_{\rm b}$, the structure equations are solved at every time step. The thermal evolution Equations (1) and (2) are solved in the whole star, i.e., from the center down to $\rho_{\rm b}$, at every time step.

So, in the inner envelope, structure and thermal evolution equations have to be solved at each time step. There are several ways to do this, and we tried some of them until we found a suitable one. The most considerable difficulty lies in the fact that the outer parts of the inner envelope are dominated by photons and electron–positron pairs. Thus, the adiabatic index is close to 4/3, and the system is close to being unstable.

In the standard long-term cooling calculation scheme (see, e.g., Page 1989; Gnedin et al. 2001), thermal evolution equations are usually solved fully implicitly by employing Newton–Raphson method (Henyey scheme Henyey et al. 1959). The easiest way to modify this scheme to handle neo-neutron stars is to solve structure equations separately from thermal equations at each Newton–Raphson iteration for the thermal equations. Unfortunately, this idea does not work. The thermal Equation (2) (which is basically the energy conservation law) and the hydrostatic equilibrium equation (Equation (4) of Potekhin & Chabrier 2018) have a tendency to create oscillations in pressure, radius, and temperature. This is easy to understand: if we solve them separately, some decrease in the radius will cause an increase in the temperature due to the injection of contraction energy (Equation (2)), which will increase the pressure and cause an increase in the radius due to the hydrostatic equilibrium equation. This will, in turn, cause the temperature and pressure to drop and a decrease in the radius. Clearly, this method is prone to instability and should not be used. We implemented it and found out that it indeed resulted in diverging iterations and in oscillations.

So, to deal with this tendency to oscillate, one has to solve structure and thermal equations together in a single Newton–Raphson iteration scheme. In this case, the changes in the pressure, radius, and temperature are coordinated with each other at each iteration and consistent solution can be obtained. As it turns out there is no need to solve all six equations together in a single Newton–Raphson scheme. Actually, it is sufficient to solve only four equations (Equations (1) and (2) here and Equations (1) and (4) from Potekhin & Chabrier 2018) together, and Equations (2) and (3) from Potekhin & Chabrier (2018) can be solved separately as they do not produce any oscillations. We implemented this approach, and it worked.

However, the iterations converged slowly and not for all initial conditions.

So, we improved our solver further and implemented the "globally convergent" Newton scheme of Press et al. (2007), which employed backtracking line searches. It improved the situation. The iterations converged faster. But still the number of iterations for early time steps was 5–10 times bigger than in the standard long-term cooling. Probably, some even more elaborate solver can improve the situation yet it looks like there is not much more. The alternative is to switch from a sequence of hydrostatic equilibria to a hydrodynamic calculation in full GR, but this is far beyond the scope of the current paper.

Another numerical complication is the necessity to match the initial and boundary conditions. For the standard long-term cooling, it is possible to start with a constant (redshifted) temperature profile (thus, zero luminosity inside, which is inconsistent with a nonzero surface luminosity, i.e., $L_{\rm s} \neq L_{\rm b}$) and the matching will occur automatically at the first time step. In our neo-neutron star models, the Henyey method would not converge at the first time step if such inconsistent surface luminosity is employed. So, we have developed a special matching procedure for the luminosity to start with consistent initial and boundary conditions: $T_{t=0}(\rho) = F(\rho, \{p_1, p_2, \ldots\}, p_{\rm match})$, where $p_1, p_2, \ldots, p_{\rm match}$ are free parameters of the parameterization of an arbitrary initial temperature profile. The procedure is as follows: we fix the values of $p_1, p_2, \ldots$ and use the Newton–Raphson method to search for the value of $p_{\rm match}$ until the initial profile satisfies the boundary condition to the desired precision [i.e., we stop when $L_{\rm s}\{T_{\rm s}(T_{\rm b})\} = L_{\rm b}$]. Typically, this takes five to six Newton–Raphson iterations. Employment of such a procedure means that our initial temperature profile is no longer completely arbitrary.

In particular, as an initial temperature, we take a uniform value T_0 at densities above $\rho_{\rm c}$, and in the inner envelope, we choose

$$T_0(\rho) = T_{\rm c,0} - \Delta T \left(\frac{\log[\rho_{\rm c}/\rho]}{\log[\rho_{\rm c}/\rho_{\rm b}]} \right)^{\gamma} \tag{23}$$

where $\Delta T = T_{\rm c,0} - T_{\rm b}$, and $\gamma > 0$ is a power-law index. So, if γ is 1, then $T_0(\rho)$ is just linear in $\log \rho$. We usually fixed the value of $T_{\rm c,0}$ to be 2.5×10^{10} K, and for various values of γ, we solved for ΔT to match the initial and boundary conditions.

Unfortunately, with the parameterization (23), the matching occurs only at super-Eddington surface luminosities for any tested value of γ.[9] As we do not consider mass loss and stellar winds in the current work, we had two options: change the initial temperature parameterization or explicitly set the initial luminosity in the inner envelope. We decided to do the latter. Setting the initial luminosity directly requires a separate step in the algorithm to solve for the initial temperature given the initial luminosity. We incorporated matching of the initial and boundary conditions in this step. In such a scheme, we lost direct control over the initial temperature, but, as we show in Section 5, direct control over luminosity might be more useful for studying neo-neutron stars. Besides, we can still control $T_{\rm b,0}$ via $T_{\rm b}$–$T_{\rm s}$ relations and the fact that $L_{\rm s}(T_{\rm s}(T_{\rm b})) = L_{\rm b}$. We can also control $T_{\rm c,0}$ by adjusting the initial luminosity (see details in Section 5). We kept the parameterization (23) to demonstrate how a relatively small change in the initial temperature profile can considerably affect the cooling during the first $\sim 10^4$ s.

ORCID iDs

Mikhail V. Beznogov https://orcid.org/0000-0002-7326-7270
Dany Page https://orcid.org/0000-0003-2498-4326
Enrico Ramirez-Ruiz https://orcid.org/0000-0003-2558-3102

References

Abbott, B. P., Abbott, R., Abbott, T. D., et al. 2017a, ApJL, 848, L13
Abbott, B. P., Abbott, R., Abbott, T. D., et al. 2017b, ApJL, 848, L12
Akmal, A., Pandharipande, V. R., & Ravenhall, D. G. 1998, PhRvC, 58, 1804
Antoniadis, J., Freire, P. C. C., Wex, N., et al. 2013, Sci, 340, 448
Baade, W., & Zwicky, F. 1934, PNAS, 20, 254
Bahcall, J. N., Rees, M. J., & Salpeter, E. E. 1970, ApJ, 162, 737
Baiko, D. A., Kaminker, A. D., Potekhin, A. Y., & Yakovlev, D. G. 1998, PhRvL, 81, 5556
Barnes, J., & Kasen, D. 2013, ApJ, 775, 18
Bethe, H. A. 1936, PhRv, 50, 332
Beznogov, M. V., Potekhin, A. Y., & Yakovlev, D. G. 2016, MNRAS, 459, 1569
Beznogov, M. V., & Yakovlev, D. G. 2015, MNRAS, 447, 1598
Bildsten, L., Shen, K. J., Weinberg, N. N., & Nelemans, G. 2007, ApJL, 662, L95
Boguta, J. 1981, PhLB, 106, 255
Brown, E. F., & Cumming, A. 2009, ApJ, 698, 1020
Browne, E., & Tuli, J. K. 2013, NDS, 114, 1849
Bucurescu, D., & von Egidy, T. 2015, EPJWC, 93, 06003
Burrows, A., & Lattimer, J. M. 1986, ApJ, 307, 178
Canal, R., Garcia, D., Isern, J., & Labay, J. 1990, ApJL, 356, L51
Canal, R., & Schatzman, E. 1976, A&A, 46, 229
Cigan, P., Matsuura, M., Gomez, H. L., et al. 2019, ApJ, 886, 51
Coulter, D. A., Foley, R. J., Kilpatrick, C. D., et al. 2017, Sci, 358, 1556
Cromartie, H. T., Fonseca, E., Ransom, S. M., et al. 2019, NatAs, in press
Darbha, S., Metzger, B. D., Quataert, E., et al. 2010, MNRAS, 409, 846
Demorest, P. B., Pennucci, T., Ransom, S. M., Roberts, M. S. E., & Hessels, J. W. T. 2010, Natur, 467, 1081
Dessart, L., Burrows, A., Ott, C. D., et al. 2006, ApJ, 644, 1063
Eichler, D., Livio, M., Piran, T., & Schramm, D. N. 1989, Natur, 340, 126
Faber, J. A., & Rasio, F. A. 2012, LRR, 15, 8
Fesen, R. A., Hammell, M. C., Morse, J., et al. 2006, ApJ, 645, 283
Folatelli, G., Bersten, M. C., Benvenuto, O. G., et al. 2014, ApJL, 793, L22
Fong, W., Berger, E., Blanchard, P. K., et al. 2017, ApJL, 848, L23
Geppert, U., Küker, M., & Page, D. 2004, A&A, 426, 267
Geppert, U., Küker, M., & Page, D. 2006, A&A, 457, 937
Gilbert, A., & Cameron, A. G. W. 1965, CaJPh, 43, 1446
Gnedin, O. Y., Yakovlev, D. G., & Potekhin, A. Y. 2001, MNRAS, 324, 725
Greenstein, G., & Hartke, G. J. 1983, ApJ, 271, 283
Gudmundsson, E. H., Pethick, C. J., & Epstein, R. I. 1982, ApJL, 259, L19
Haensel, P., Potekhin, A. Y., & Yakovlev, D. G. 2007, Neutron Stars. I. Equation of State and Structure, Astrophysics and Space Science Library, Vol. 326 (New York: Springer)
Haensel, P., Zdunik, J. L., & Dobaczewski, J. 1989, A&A, 222, 353
Hansen, C. J., Kawaler, S. D., & Trimble, V. 2004, Stellar Interiors: Physical Principles, Structure, and Evolution (New York: Spinger)
Henyey, L. G., Wilets, L., Böhm, K. H., Lelevier, R., & Levee, R. D. 1959, ApJ, 129, 628
Huizenga, J. R., & Moretto, L. G. 1972, ARNPS, 22, 427
Itoh, N., Hayashi, H., Nishikawa, A., & Kohyama, Y. 1996, ApJS, 102, 411
Janka, H.-T. 2012, ARNPS, 62, 407
Junde, H., Su, H., & Dong, Y. 2011, NDS, 112, 1513
Kaminker, A. D., Pethick, C. J., Potekhin, A. Y., Thorsson, V., & Yakovlev, D. G. 1999, A&A, 343, 1009
Kaminker, A. D., & Yakovlev, D. G. 1994, ARep, 38, 809
Kaplan, D. L., Frail, D. A., Gaensler, B. M., et al. 2004, ApJS, 153, 269
Kaplan, D. L., Gaensler, B. M., Kulkarni, S. R., & Slane, P. O. 2006, ApJS, 163, 344
Kasen, D., Metzger, B., Barnes, J., Quataert, E., & Ramirez-Ruiz, E. 2017, Natur, 551, 80

---

[9] Of course, with the surface boundary condition (7), we cannot have super-Eddington surface luminosity; thus, we had to extrapolate the $T_{\rm b}$–$T_{\rm s}$ relations of Section 3.1 to higher temperatures to obtain the matching.

Kaspi, V. M., & Beloborodov, A. M. 2017, ARA&A, 55, 261
Kilpatrick, C. D., Foley, R. J., Kasen, D., et al. 2017, Sci, 358, 1583
Kippenhahn, R., Weigert, A., & Weiss, A. 2012, Stellar Structure and Evolution (Berlin: Springer)
Kluźniak, W., & Ruderman, M. 1998, ApJL, 505, L113
Landau, L. D., & Lifshitz, E. M. 1993, Statistical Physics: I (Oxford: Pergamon)
Lattimer, J. M., Pethick, C. J., Prakash, M., & Haensel, P. 1991, PhRvL, 66, 2701
Lattimer, J. M., & Swesty, D. F. 1991, NuPhA, 535, 331
Lattimer, J. M., van Riper, K. A., Prakash, M., & Prakash, M. 1994, ApJ, 425, 802
Lee, W. H., & Ramirez-Ruiz, E. 2007, NJPh, 9, 17
Livne, E., Asida, S. M., & Höflich, P. 2005, ApJ, 632, 443
Lopez, L. A., Ramirez-Ruiz, E., Castro, D., & Pearson, S. 2013, ApJ, 764, 50
Lopez, L. A., Ramirez-Ruiz, E., Huppenkothen, D., Badenes, C., & Pooley, D. A. 2011, ApJ, 732, 114
Margalit, B., & Metzger, B. D. 2017, ApJL, 850, L19
Margutti, R., Alexander, K. D., Xie, X., et al. 2018, ApJL, 856, L18
Margutti, R., Berger, E., Fong, W., et al. 2017, ApJL, 848, L20
Maund, J. R., & Smartt, S. J. 2009, Sci, 324, 486
Maund, J. R., Smartt, S. J., Kudritzki, R. P., Podsiadlowski, P., & Gilmore, G. F. 2004, Natur, 427, 129
Metzger, B. D., Martínez-Pinedo, G., Darbha, S., et al. 2010, MNRAS, 406, 2650
Metzger, B. D., Piro, A. L., & Quataert, E. 2009, MNRAS, 396, 1659
Metzger, B. D., Quataert, E., & Thompson, T. A. 2008, MNRAS, 385, 1455
Metzger, B. D., Thompson, T. A., & Quataert, E. 2018, ApJ, 856, 101
Miller, M. C. 1995, ApJL, 448, L29
Miyaji, S., Nomoto, K., Yokoi, K., & Sugimoto, D. 1980, PASJ, 32, 303
Murguia-Berthier, A., Montes, G., Ramirez-Ruiz, E., De Colle, F., & Lee, W. H. 2014, ApJL, 788, L8
Murguia-Berthier, A., Ramirez-Ruiz, E., Kilpatrick, C. D., et al. 2017, ApJL, 848, L34
Nakar, E. 2007, PhR, 442, 166
Nakazato, K., Suzuki, H., & Togashi, H. 2018, PhRvC, 97, 035804
Nomoto, K., & Kondo, Y. 1991, ApJL, 367, L19
Nomoto, K., & Tsuruta, S. 1987, ApJ, 312, 711
Page, D. 1989, PhD thesis, State Univ. New York at Stonybrook
Page, D. 1995, ApJ, 442, 273
Page, D. 2016, NSCool: Neutron star cooling code, Astrophysics Source Code Library, ascl:1609.009
Page, D., & Applegate, J. H. 1992, ApJL, 394, L17
Page, D., Geppert, U., & Weber, F. 2006, NuPhA, 777, 497
Page, D., Lattimer, J. M., Prakash, M., & Steiner, A. W. 2004, ApJS, 155, 623
Page, D., Lattimer, J. M., Prakash, M., & Steiner, A. W. 2009, ApJ, 707, 1131
Page, D., Prakash, M., Lattimer, J. M., & Steiner, A. W. 2011, PhRvL, 106, 081101
Page, D., & Reddy, S. 2012, in Neutron Star Crust, ed. C. A. Bertulani & J. Piekarewicz (Hauppauge, NY: Nova Science), 281
Page, D., & Sarmiento, A. 1996, ApJ, 473, 1067
Pérez-Azorín, J. F., Miralles, J. A., & Pons, J. A. 2006, A&A, 451, 1009
Pons, J. A., Reddy, S., Prakash, M., Lattimer, J. M., & Miralles, J. A. 1999, ApJ, 513, 780
Potekhin, A. Y., Baiko, D. A., Haensel, P., & Yakovlev, D. G. 1999, A&A, 346, 345
Potekhin, A. Y., & Chabrier, G. 2010, CoPP, 50, 82
Potekhin, A. Y., & Chabrier, G. 2018, A&A, 609, A74
Potekhin, A. Y., Pons, J. A., & Page, D. 2015, SSRv, 191, 239
Potekhin, A. Y., & Yakovlev, D. G. 2001, A&A, 374, 213
Poutanen, J. 2017, ApJ, 835, 119
Press, W. H., Teukolsky, S. A., Vetterling, W. T., & Flannery, B. P. 2007, Numerical Recipes. The Art of Scientific Computing (3rd ed.; Cambridge: Cambridge Univ. Press)
Price, D. J., & Rosswog, S. 2006, Sci, 312, 719
Ramirez-Ruiz, E., Andrews, J. J., & Schrøder, S. L. 2019, ApJL, 883, L6
Rezzolla, L., Giacomazzo, B., Baiotti, L., et al. 2011, ApJL, 732, L6
Rezzolla, L., Most, E. R., & Weih, L. R. 2018, ApJL, 852, L25
Roberts, L. F., Kasen, D., Lee, W. H., & Ramirez-Ruiz, E. 2011, ApJL, 736, L21
Rosswog, S., & Liebendörfer, M. 2003, MNRAS, 342, 673
Rosswog, S., Ramirez-Ruiz, E., & Davies, M. B. 2003, MNRAS, 345, 1077
Ruiter, A. J., Ferrario, L., Belczynski, K., et al. 2019, MNRAS, 484, 698
Schatz, H., Bildsten, L., Cumming, A., & Wiescher, M. 1999, ApJ, 524, 1014
Shibata, M., Zhou, E., Kiuchi, K., & Fujibayashi, S. 2019, PhRvD, 100, 023015
Tananbaum, H. 1999, IAUC, 7246
Thompson, C., & Duncan, R. C. 1995, MNRAS, 275, 255
Usov, V. V. 1992, Natur, 357, 472
Villar, V. A., Guillochon, J., Berger, E., et al. 2017, ApJL, 851, L21
von Egidy, T., & Bucurescu, D. 2005, PhRvC, 72, 044311
von Egidy, T., & Bucurescu, D. 2009, PhRvC, 80, 054310
Wang, B. 2018a, RAA, 18, 049
Wang, B. 2018b, MNRAS, 481, 439
Woosley, S. E., & Baron, E. 1992, ApJ, 391, 228
Yakovlev, D. G., & Kaminker, A. D. 1994, in IAU Coll. 147, The Equation of State in Astrophysics, ed. G. Chabrier & E. Schatzman (Cambridge: Cambridge Univ. Press), 214
Yakovlev, D. G., & Pethick, C. J. 2004, ARA&A, 42, 169
Yakovlev, D. G., & Urpin, V. A. 1980, SvA, 24, 303